

WING FLUTTER ANALYSIS WITH AN UNCOUPLED METHOD

A THESIS SUBMITTED TO
THE GRADUATE SCHOOL OF NATURAL AND APPLIED SCIENCES
OF
THE MIDDLE EAST TECHNICAL UNIVERSITY

BY

KORAY KAVUKCUOĞLU

IN PARTIAL FULFILLMENT OF THE REQUIREMENTS FOR THE DEGREE OF
MASTER OF SCIENCE
IN
THE DEPARTMENT OF AEROSPACE ENGINEERING

AUGUST 2003

Approval of the Graduate School of Natural and Applied Sciences

Prof. Dr. Canan ÖZGEN

Director

I certify that this thesis satisfies all the requirements as a thesis for the degree of Master of Science.

Prof. Dr. Nafiz ALEMDAROĞLU

Head of Department

This is to certify that we have read this thesis and that in our opinion it is fully adequate, in scope and quality, as a thesis for the degree of Master of Science.

Dr. Erdal OKTAY

Co-Supervisor

Prof. Dr. Mehmet A. AKGÜN

Supervisor

Examining Committee Members

Prof. Dr. Mehmet A. AKGÜN

Assoc. Prof. Dr. Sınan EYİ

Assoc. Prof. Dr. Serkan ÖZGEN

Assist. Prof. Dr. Altan KAYRAN

Dr. Erdal OKTAY

ABSTRACT

WING FLUTTER ANALYSIS WITH AN UNCOUPLED METHOD

Kavukcuoğlu, Koray

M.Sc., Department of Aerospace Engineering

Supervisor: Prof. Dr. Mehmet A. AKGÜN

Co-Supervisor: Dr. Erdal OKTAY

August 2003, 87 pages

In this thesis, flutter of AGARD Wing 445.6 is predicted with a new approach. The unsteady aerodynamic loads are calculated with an unstructured Euler solver. Surface interpolation is used to transfer the calculated mode shapes from the structural mesh to the CFD mesh and to transfer pressure distributions in the opposite direction. Using the transferred pressure distributions, nodal force distributions on the finite element model are calculated. A polynomial is fitted to the nodal forces in terms of the reduced frequency. The resulting polynomial eigenvalue problem is solved to obtain flutter frequency.

Keywords: Aeroelasticity, Flutter, AGARD Wing 445.6, CFD, Computational Fluid Dynamics.

ÖZ

YAPISAL VE AKIŞ PROBLEMLERİNİN AYRI ÇÖZÜLDÜĞÜ BİR YÖNTEM İLE KANAT ÇIRPINTI ANALİZİ

Kavukcuoğlu, Koray

Yüksek Lisans, Havacılık Mühendisliği Bölümü

Tez Yöneticisi: Prof. Dr. Mehmet A. AKGÜN

Ortak Tez Yöneticisi: Dr. Erdal OKTAY

Ağustos 2003, 87 sayfa

Bu tezde, yeni bir yaklaşım kullanılarak AGARD 445.6 kodlu kanadın çırıntı analizi yapılmıştır. Üç boyutlu bir Euler çözümü kullanılarak sinüssel aerodinamik kuvvetler hesaplanmıştır. Yüzey interpolasyonu kullanılarak yapısal modelde hesaplanmış doğal titreşim şekilleri SAD (Sayısal Akışkanlar Dinamiği) modeline ve SAD modelinde hesaplanmış basınç dağılımları yapısal modele aktarılmıştır. Aktarılan basınç dağılımı kullanılarak, yapısal model üzerinde kuvvet dağılımı elde edilmiştir. Modelin düğüm noktalarına etkiyen kuvvetlere boyutsuz frekans cinsinden bir polinom uydurulmuş ve elde edilen polinom özdeğer problemi çözülerek yapının çırıntı frekansı hesaplanmıştır.

Anahtar Kelimeler: Aeroelastisite, Çırıntı, AGARD Wing 445.6, SAD, Sayısal Akışkanlar Dinamiği.

To My Wife

ACKNOWLEDGEMENTS

I wish to express my appreciation to Prof. Dr. Mehmet A. AKGÜN for his continuous and strong guidance, supervision and encouragement in the preparation of this thesis and I would like to thank Dr. Erdal OKTAY for his support.

I would like to thank ROKETSAN Missiles Industries Inc. and Engineering Development Department for their support.

I am grateful to my elder brother Çağatay for his invaluable support. I also would like to thank Mr. Bayındır KURAN and Dr. Sartuk KARASOY for their encouragement. In addition, I would like to thank my parents for their moral guidance and my friends, especially Ms. F. Demet ÜLKER, for their great friendship and support which helped me a lot during the preparation of this thesis. Finally, I would like to thank my wife Beril, I know that I could not finish this thesis without her.

TABLE OF CONTENTS

ABSTRACT	iii
ÖZ.....	iv
ACKNOWLEDGEMENTS.....	vi
TABLE OF CONTENTS	vii
LIST OF SYMBOLS.....	ix
CHAPTER	
1 INTRODUCTION	1
2 FLUTTER MODELING.....	7
2.1 Introduction	7
2.2 Flutter Modeling of a One-Degree-of-Freedom System.....	8
2.3 Flutter Modeling of a Two-Degree-of-Freedom System	9
2.4 P-K Method	11
2.5 Coupled CFD-CSD Methods.....	13
2.6 Method Used in This Study.....	14
3 MODAL ANALYSIS OF AGARD WING 445.6	20

3.1 Introduction	20
3.2 Finite Element Model.....	20
3.3 Modal Analysis.....	23
4 AERODYNAMIC ANALYSIS OF AGARD WING 445.6.....	30
4.1 Introduction	30
4.2 Theory of USER3D Computational Fluid Dynamics Solver	30
4.3 Moving Mesh Algorithm.....	34
4.4 Computational Fluid Dynamics Model.....	36
4.5 Solution Procedure.....	41
4.6 Grid Transformation Between CFD and Solid Models	44
4.7 CFD Solution Results.....	47
4.8 Force Calculation on the Structural Model	59
4.9 Aerodynamic Loading on Structural Model.....	66
5 NUMERICAL SOLUTION	69
5.1 Introduction	69
5.2 Solution Procedure.....	70
6 SUMMARY, CONCLUSIONS AND RECOMMENDATIONS	78
REFERENCES.....	80
APPENDICES	
A. LIFT COEFFICIENT VARIATIONS	83
B. ANSYS FINITE MODEL MACRO FILE	86

LIST OF SYMBOLS

ω_F	: Flutter frequency
U_F	: Flutter speed
U, V	: Freestream velocity
α	: Angle of attack
h	: Vertical displacement
\bar{h}_0	: Amplitude of vertical oscillation
$\bar{\alpha}_0$: Amplitude of angular oscillation
ω	: Oscillation frequency
t	: Time
ϕ	: Phase difference
I_α	: Mass moment of inertia
K_α	: Torsional spring stiffness constant
M_y	: Aerodynamic moment
m	: Mass
w_h	: Uncoupled natural bending frequency
w_α	: Uncoupled natural torsional frequency
Q_h	: Aerodynamic force in the vertical direction
Q_α	: Aerodynamic moment about the aerodynamic center
S_α	: Static mass moment per unit span
L	: Lift

$[M]$: Mass matrix
$[K]$: Stiffness matrix
$\{f\}$: Aerodynamic force function
$\{q\}$: Displacement
$\{\eta\}, \{u\}$: Generalized displacement
$[\Phi]$: Mass normalized mode shape
k	: reduced frequency
ρ	: density
b	: reference semi-chord
γ, ζ	: Damping coefficient
$[M_M], [M_h]$: Modal mass matrix
$[K_M], [K_h]$: Modal stiffness matrix
$\{\bar{\eta}\}$: complex displacement vector

CHAPTER 1

INTRODUCTION

Aeroelasticity can be defined as a science which studies the interaction between inertial forces, aerodynamic forces and elastic forces [1]. The aeroelastic problems can be classified by means of a modified Collar triangle as shown in Figure 1.1. Flutter is defined as the dynamic instability of an elastic body in an airstream [1]; it is caused by the unsteady aerodynamic forces generated from elastic deformations of the structure.

Flutter problem has been of great interest since early years of flight. Theodorsen has investigated the mechanism of flutter by formulating it through pitching and plunging motion of airfoils in two dimensional flows in 1934 [2]. Comparison of experimental data with the theoretical solution is given in [3] by Theodorsen and Garrick. At early times the aerodynamic forces were formulated by one dimensional piston theory [4] which was first formulated by Ashley and Zartarian, or strip theory. The most common application of the strip theory was formulated as modified strip theory by Yates [5].

As the computational capabilities have increased, the complexity of aerodynamic models used in flutter analysis has grown rapidly. The solution procedures have changed from uncoupled solutions to coupled solutions. Major steps of coupled algorithms are given in Figure 1.2.

Coupled aeroelastic solution procedures can be categorized into three groups as fully coupled algorithms, strongly coupled algorithms and weakly coupled algorithms.

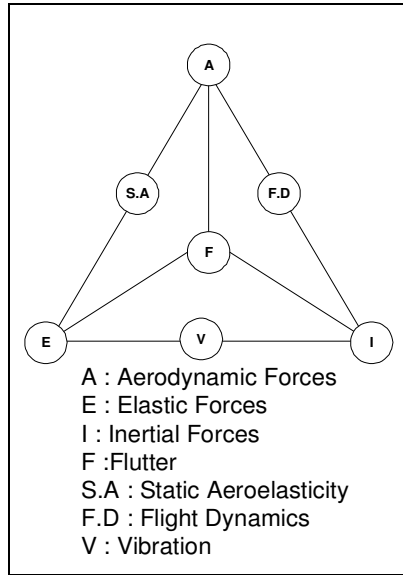


Figure 1.1 Modified Collar Triangle

In the case of fully coupled algorithms, the complete system involving fluid and structure solver is embedded into a unique code. For this case an iterative solution is carried out at each time step. Strongly coupled algorithms contain sufficient interaction between the two codes such that the stability of the system is at least equal to that of the least stable code. Weakly coupled algorithms usually consist of two separate programs which are connected to each other through a defined interface. Coupling between the two codes is done once for each time step [6].

Aerodynamic formulations used in aeroelastic analysis have evolved to 3D Euler and Navier-Stokes solvers. Recently, flutter calculations of three dimensional structures using Euler and Navier-Stokes solutions in a fully coupled algorithm are presented by Lee and Batina [7], [8]. Liu, Cai, Zhu developed a strongly coupled

Computational Fluid Dynamics (CFD)/Computational Structural Dynamics (CSD) method for predicting flutter boundaries using Euler/Navier-Stokes equations [19].

All of the above studies present coupled algorithms in different manners. However, the nature of the coupled algorithms requires that fluid and structure codes be run at each time step and data needs to be interchanged between the two. Although CPU times and resources required by structural codes are low, this is not the case for computational fluid mechanics solvers. As a result, a large computational effort is required for solution of aeroelastic problems.

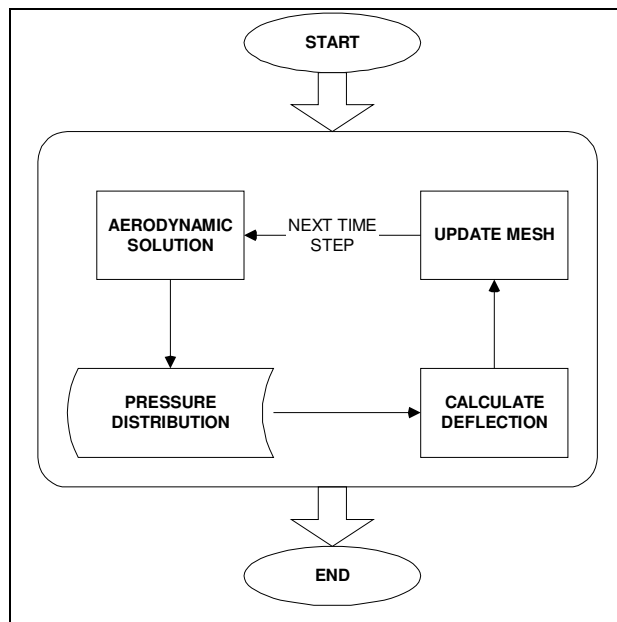


Figure 1.2 Coupled Aeroelastic Solution Procedure

In this thesis, a new approach will be presented for solution of aeroelastic problems, which is proposed by Akgün [16]. It is a variant of uncoupled algorithms which formulate the problem as an eigenvalue problem. The aim is to decouple the structural and fluid solvers, but link them suitably. The connection will be maintained not by coupling of two codes, but by computing the aerodynamic forces at the mode shapes of the structure at a number of frequencies in order to use them at any condition.

The flowchart of the solution procedure is given below in Figure 1.3. The major steps of the solution A through C are carried out independently, but solution of each step is transferred to the next. The first step (STEP A) is to carry out the modal analysis of the structure. This step is carried out with the commercial finite element analysis tool ANSYS® and verified with MATLAB®. The mode shapes and modal frequencies of the structure are stored for aerodynamic analysis.

The next step (STEP B) is to carry out the aerodynamic solution of the geometry. Unsteady aerodynamic solution is performed at a number of frequencies in a certain range at each mode shape of the structure. The “modal” aerodynamic forces generated from the deflected shape of the structure are stored at each time step to be used in flutter analysis. The unsteady aerodynamic solution is carried out with USER3D (3 Dimensional Unsteady Parallel Euler Solver) developed by Oktay [12].

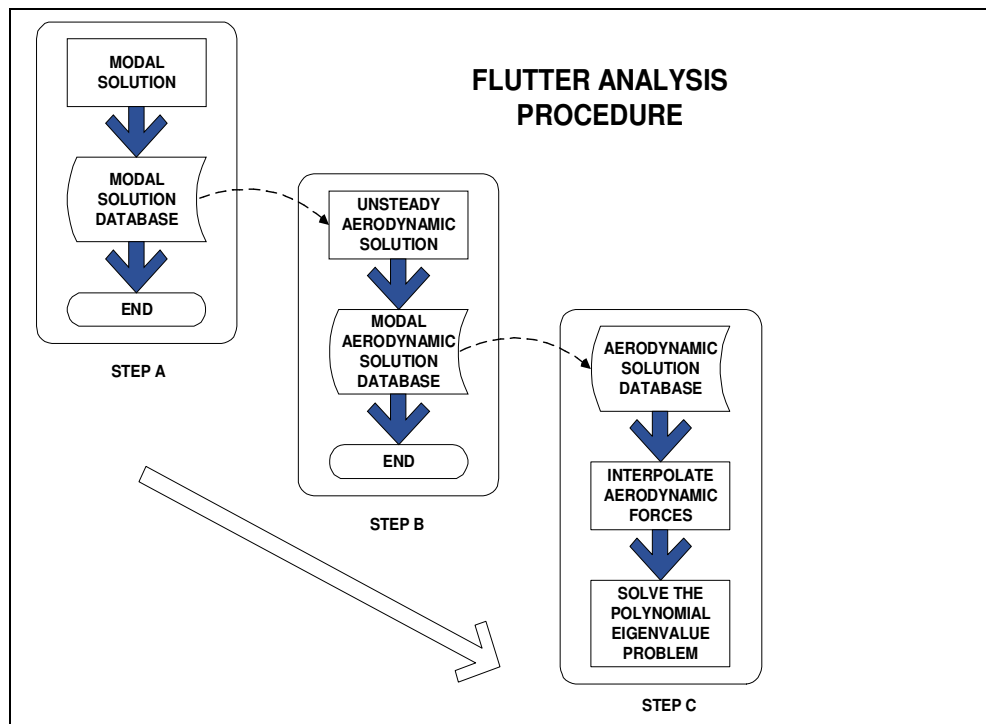


Figure 1.3 Solution Procedure Used in the Thesis [16]

The third step (STEP C) is to carry out the flutter analysis. The aerodynamic solution database stored in the previous step is utilized to extract aerodynamic forces at any frequency through polynomial interpolation functions. The element matrices that have been extracted from ANSYS and the aerodynamic force matrices are used in a polynomial eigenvalue problem solved with MATLAB. Surface spline fitting technique is implemented for transforming pressure distribution to force distribution between the aerodynamic solution domain and the structural solution domain.

This procedure eliminates the need for coupling of fluid and structural codes and the number of aerodynamic solutions required is decreased greatly. With this procedure, aerodynamic solution is required at a number of frequencies at each mode shape involved. The aerodynamic solution step does not require on-line interaction with the structural model and parallel computing can be used to generate the unsteady load database. Parallel processing facility of the Aerospace Engineering Department and of ROKETSAN Missile Industries inc. were used for that purpose.

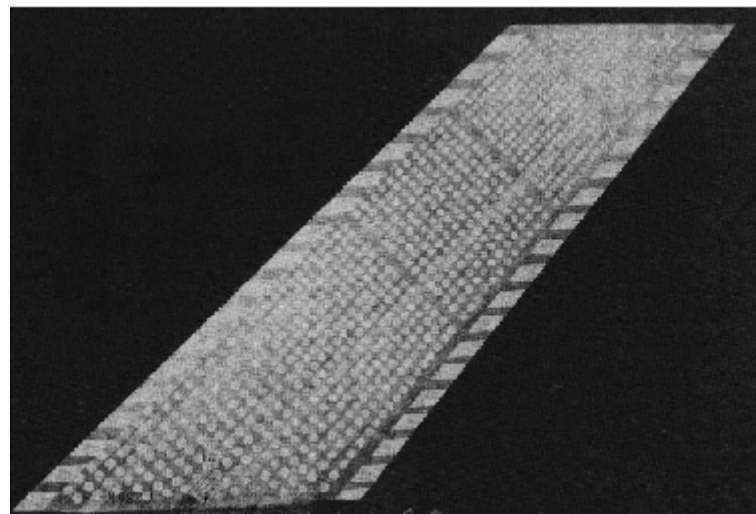


Figure 1.4 AGARD Wing 445.6, Weakened Model

The proposed methodology is applied to AGARD Aeroelastic Wing 445.6 [9], since theoretical solution of and experimental work on this wing are documented in detail. The modal frequencies and shapes of the structure are compared with experimental results [9], solution of Kolonay [10], and Li [11].

AGARD Aeroelastic wing has a 45 degree sweep angle and a taper ratio of 0.6. The streamwise cross-section of the wing is NACA65004 airfoil. The chord length at the root is 22 inches, at the tip 14.5 inches and the span is 30 inches. There are two configurations of the wing, solid and weakened. In this thesis, the weakened model is used as the reference case. The wing model is shown in Figure 1.4.

In Chapter 2, flutter modeling is discussed starting with simplest models and the approach used in this study is explained. The modal analysis of the wing is discussed in Chapter 3, the aerodynamic method is given in Chapter 4 together with the aerodynamic results. In Chapter 5, the numerical application of flutter analysis procedure is given with the results and comparison with previous studies. Chapter 6 includes the summary, conclusions, and recommendations for future work.

CHAPTER 2

FLUTTER MODELING

2.1 Introduction

Flutter is generally observed on wings and control surfaces since these types of structures are subject to large aerodynamic loads. Flutter is produced due to forces that are generated from the dynamic deflections of an elastic structure from the undeformed state [1].

Flutter is defined by a critical speed U_F and critical frequency ω_F . U_F is the lowest air speed and ω_F is the corresponding circular frequency at which a given structure flying at a given atmospheric condition will undergo sustained, simple harmonic oscillations. The solution of flutter leads to a complex eigenvalue problem where two characteristic numbers determine the speed and frequency.

The flutter problem has been modeled in various ways starting from single degree of freedom models to CFD – CSD coupled solutions. In this chapter, models proposed by various investigators will be presented in order to explain the development in flutter modeling. The approach proposed by Akgün [16] will be explained. In the following chapters, the application of this method with a CFD solver will be presented.

2.2 Flutter Modeling of a One-Degree-of-Freedom System

The very basic approach to flutter problem is modeling of a rigid airfoil of unit span [1]. The airfoil is assumed to be hinged at the leading edge by a torsional spring as shown in Figure 2.1. The undeformed position of the airfoil is assumed to be zero degrees of angle of attack in a low-speed air flow.

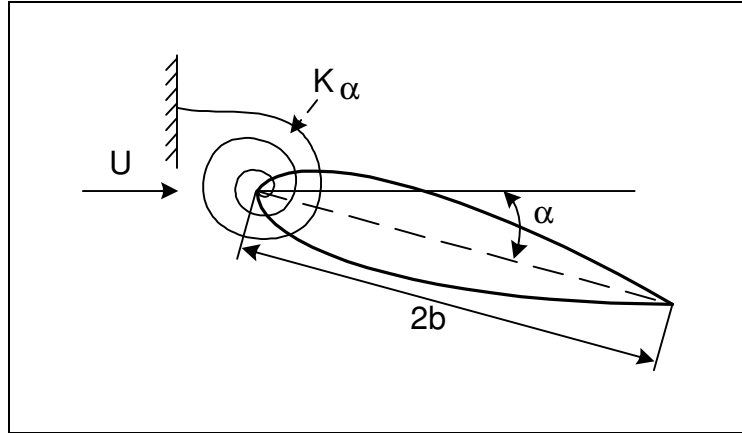


Figure 2.1. Single DOF Flutter Model

The stiffness constant of the torsional spring is denoted by K_α , α is the AOA (Angle of Attack). The equation of motion for this system is

$$I_\alpha \ddot{\alpha} + K_\alpha \alpha = M_y \quad (2.1)$$

where I_α is the moment of inertia about the leading edge, M_y is the aerodynamic moment due to $\alpha(t)$ at the leading edge. The oscillation of the airfoil is assumed to be harmonic oscillation with a frequency of ω , amplitude $\bar{\alpha}_0$ and time t

$$\alpha = \bar{\alpha}_0 e^{i\omega t} \quad (2.2)$$

Solving equation 2.1 requires an appropriate substitution for aerodynamic forces. After formulation of aerodynamic forces, flutter frequency and speed can be solved. The formulation of unsteady aerodynamic forces can be done according to piston theory [4], or strip theory [5] or another unsteady formulation. These formulations all emerge from the potential flow theory with small disturbance assumption.

Flutter modeling of a complex structure often requires much more detailed models than a single DOF model. In the next section, a two DOF model will be presented for reference.

2.3 Flutter Modeling of a Two-Degree-of-Freedom System

The next level of an example flutter modeling would be a two DOF system [1]. The system consists of a rigid airfoil of unit span as in the previous case but in addition to torsional motion, bending will also be included in the model. This model coincides with the solutions given in references [2], [3].

The Lagrange formulation for the model shown in Figure 2.2 is

$$m\ddot{h} + S_\alpha \dot{\alpha} + mw_h^2 h = Q_h \quad (2.3)$$

$$S_\alpha \ddot{h} + I_\alpha \ddot{\alpha} + I_\alpha w_\alpha^2 \alpha = Q_\alpha \quad (2.4)$$

Q_h and Q_α are aerodynamic force in the vertical direction and aerodynamic moment about the aerodynamic center, respectively. m is the mass per unit span, I_α is the mass moment of inertia, S_α is the static mass moment per unit span, w_h

is the uncoupled natural bending frequency, w_α is the uncoupled natural torsional frequency.

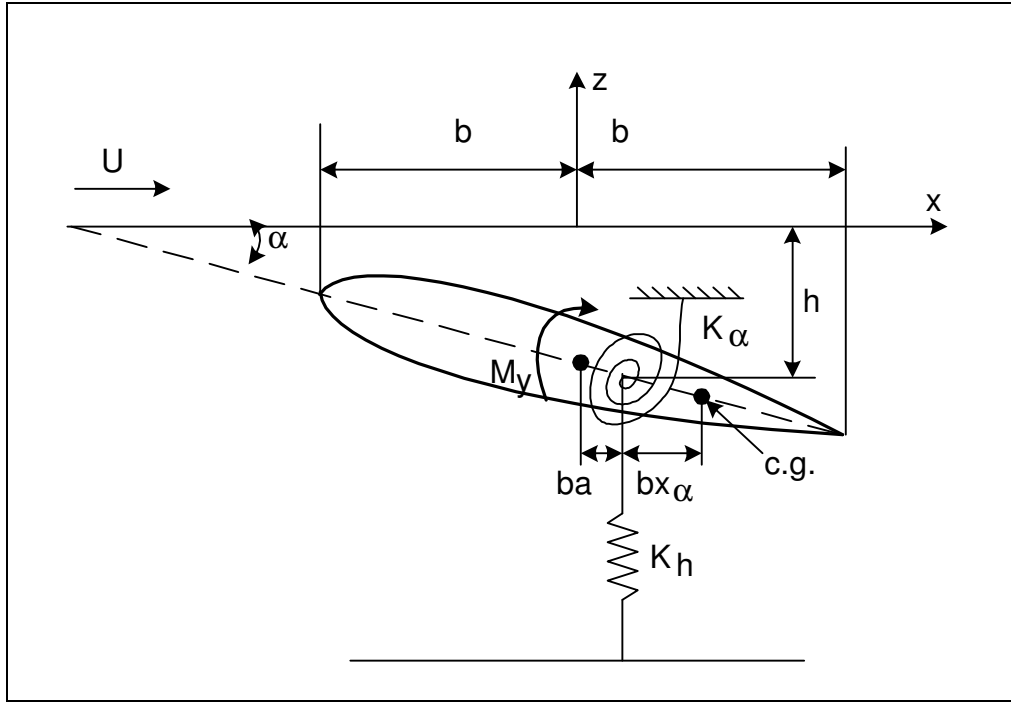


Figure 2.2. Two DOF Flutter Model

The bending motion h , and torsional motion α are assumed to be harmonic and there exists a phase shift between bending and torsional motion due to aerodynamic loads.

$$h = \bar{h}_0 e^{i\omega t} \quad (2.5)$$

$$\alpha = \bar{\alpha}_0 e^{i(\omega t + \phi)} \quad (2.6)$$

Substituting Eq. (2.5) and Eq. (2.6) into Eq. (2.3) and Eq. (2.4), we get

$$-w^2 mh - w^2 S_\alpha \alpha + mw_h^2 h = -L \quad (2.7)$$

$$-w^2 S_\alpha h - w^2 I_\alpha \alpha + I_\alpha w_\alpha^2 \alpha = M_y \quad (2.8)$$

where L is the lift and M_y is the aerodynamic moment around aerodynamic center.

By the appropriate formulation of aerodynamic forces and moments, the flutter frequency and speed can be obtained from solution of the resulting equations.

2.4 P-K Method

In this method, the flutter problem is formulated again like forced response analysis equations and solved as an eigenvalue problem [10]. The aerodynamic forces are formulated as a function of time, displacement, velocity and acceleration of the structure. Neglecting the structural damping in the structure, and denoting the mass matrix by $[M]$, stiffness matrix by $[K]$ and displacement by $\{q\}$

$$[M]\{\ddot{q}\} + [K]\{q\} = \{f(q, \dot{q}, \ddot{q}, t)\} \quad (2.9)$$

The aerodynamic forces can be separated into two parts, one being an explicit function of time only and the other a function of motion only [10].

$$\{f(q, \dot{q}, \ddot{q}, t)\} = \{f(q, \dot{q}, \ddot{q})\} + \{f(t)\} \quad (2.10)$$

The time dependent portion of the aerodynamic forces need not be included in the equation since we seek the motion induced solution. Using Eq. (2.10), the system can be rewritten as

$$[M]\{\ddot{q}\} + [K]\{q\} = \frac{1}{2} \rho V^2 [Q]\{q\} \quad (2.11)$$

where $[Q]$ is the aerodynamic force matrix, ρ is the freestream density, V is the freestream velocity. The displacement variable q can be expressed in harmonic form and transformed to modal coordinates using the mode shape matrix $[\Phi]$ and modal coordinate vector $\{\eta_h\}$

$$\{q\} = [\Phi]\{\eta_h\} e^{st} \quad (2.12)$$

Substituting Eq. (2.12), the eigenvalue problem for the solution becomes

$$\left[[M_h]s^2 + [K_h] - \frac{1}{2} \rho V^2 [Q_h] \right] \{\eta_h\} = 0 \quad (2.13)$$

Eq. (2.13) is the basic eigenvalue flutter equation. In this formulation

$$s = \frac{Vk}{b}(\gamma + i) \text{ and defining } p \text{ as } p = k(\gamma + i) \quad (2.14)$$

V ; freestream speed

b ; reference semi-chord

ρ ; freestream density

k ; reduced frequency

γ ; damping

$Q_h(M, k)$; generalized aerodynamic matrix

Eq. (2.13) is valid only when damping equals zero. The flutter condition is sought by sweeping a range of speeds and calculating damping. At the point damping crosses the zero line, the flutter speed is said to be found.

2.5 Coupled CFD-CSD Methods

Coupled CFD-CSD methods require the solution of aeroelastic equations at each time step. These methods actually contain two separate programs. One of the programs is the CFD (Computational Fluid Dynamics) solver and the other is the CSD (Computational Structural Dynamics) solver. The level of integration of two codes defines the nature of the algorithm as explained in Chapter 1. If the two codes are integrated into a single program and the fluid and structural systems of equations are solved simultaneously at each time, the resulting program is said to be at least strongly coupled. It is partly a choice of computational cost to choose strongly or weakly coupled algorithms since strongly or fully coupled algorithms require much more computational resources compared to weakly coupled algorithms.

However, independent of the coupling method, there is a need for interfacing between CFD and CSD meshes. Since the element types, resolution and locations of the two solvers are completely different, every coupled program should have an interfacing algorithm in it. In this thesis the interfacing between two domains is handled through surface interpolation techniques.

Authors of Reference 19 have developed a strongly coupled algorithm for aeroelastic problems using unsteady Navier Stokes formulation. The authors have used a second order accurate, fully implicit scheme for the integration of Navier-Stokes equations.

In order to calculate the structural deformation of the structure under aerodynamic loading, modal equations are used.

$$\ddot{q}_i + 2\zeta_i \omega_i \dot{q}_i + \omega_i^2 q_i = Q_i \quad (2.15)$$

where ζ is the structural damping coefficient. The above second order equation is transformed into two first order equations and the resulting system is decoupled by diagonalization. The resulting system of equations is expressed in a similar form of Navier-Stokes equations. The total system obtained is solved at each time step resulting in a strongly coupled CFD-CSD solver. Each real time step of solution actually consists of an iterative time integration solution for both fluid and structure equations. After both of them have reached the convergence, one real time step of solution is completed.

The interfacing between CSD and CFD grids are maintained through spline methods in Reference 19. A unique transformation matrix defined by the principle of virtual work is used for both displacement and force transformation between the two solvers.

2.6 Method Used in This Study

The approach proposed by Akgün [16] is also an eigenvalue solution for the flutter problem as the P-K method is. The approach will be described in this section. It basically aims to decouple the fluid and structural solvers to reduce the computational time. The equation of motion for the flutter problem is the same as Eq. (2.9). For the application of the method, the aerodynamic forces were generated from a 3D Unsteady Euler Solver USER3D. These forces are computed as real loads, however, the formulation is in terms of complex algebraic expressions. Hence,

$$[M]\{\ddot{q}\} + [K]\{q\} = \{f(q, \dot{q}, \ddot{q})\} \quad (2.16)$$

Transforming Eq. (2.16) into modal coordinates, assuming harmonic oscillations and representing aerodynamic force vector in complex algebra.

$$\{q\} = [\Phi]\{\eta\}e^{i\omega t} \quad (2.17)$$

$$\{f(q, \dot{q}, \ddot{q})\} = [A]\{q\} \quad (2.18)$$

$$\{f\} = [A][\Phi]\{\eta\}e^{i\omega t} \quad (2.19)$$

Using Eqs. (2.17), (2.18) and (2.19), Eq. (2.16) becomes

$$-\omega^2 [M][\Phi]\{\eta\}e^{i\omega t} + [K][\Phi]\{\eta\}e^{i\omega t} = \{f\} \quad (2.20)$$

Premultiplying by $[\Phi]^T$, the transpose of the modal matrix,

$$-\omega^2 [\Phi]^T [M][\Phi]\{\eta\}e^{i\omega t} + [\Phi]^T [K][\Phi]\{\eta\}e^{i\omega t} = [\Phi]^T \{f\} \quad (2.21)$$

Defining

$$[\Phi]^T [M][\Phi] = [M_M] \quad (2.22)$$

$$[\Phi]^T [K][\Phi] = [K_M] \quad (2.23)$$

where $[M_M]$ and $[K_M]$ are the modal mass and stiffness matrices, respectively, the equation of motion becomes

$$-\omega^2 [M_M] \{\eta\} e^{i\omega t} + [K_M] \{\eta\} e^{i\omega t} = [\Phi]^T [A] [\Phi] \{\eta\} e^{i\omega t} \quad (2.24)$$

$$\{[K_M] - \omega^2 [M_M] - [\Phi]^T [A] [\Phi]\} \{\eta\} = 0 \quad (2.25)$$

The left hand side of the equation of motion as given in Eq. (2.24) is now decoupled. The method requires a database of aerodynamic solutions. For the example solved here, these solutions are obtained for a harmonically oscillating wing according to the first four mode shapes at ten different frequencies. There exists a phase shift between the aerodynamic forces and the harmonic oscillation of the structure at each node. The phase shift depends on the node location and the frequency of oscillation.

The aerodynamic forces from the CFD code are defined in the following form.

$$\{f\}_j = \text{Im}([A]\{\phi_j\} e^{i\omega t}) \quad (2.26)$$

$$\{f\}_j = \begin{bmatrix} f_{j1} \sin(\omega t - \theta_{j1}) \\ f_{j2} \sin(\omega t - \theta_{j2}) \\ \vdots \\ f_{jN} \sin(\omega t - \theta_{jN}) \end{bmatrix} \quad (j = 1 \dots 10) \quad (2.27)$$

$$\{f\}_j = \text{Im}(\{r_j\} e^{i\omega t}) \quad (2.28)$$

$$\{r_j\} = [A]\{\phi_j\} \quad (2.29)$$

Rearranging Eq. (2.25) and using Eq. (2.29), we get the following equation.

$$\{[K_M] - \omega^2 [M_M] - [\Phi]^T [R]\} \{\eta\} = 0 \quad (2.30)$$

Where $\{r_j\}$ is a complex vector. The modulus and angle of the complex elements of $\{r_j\}$ vector are functions of ω (oscillation frequency) and the Mach number. In order to get $\{r_j\}$ vector, the aerodynamic force vector $\{f_j\}$ is multiplied by sine and cosine functions and integrated over a period of time.

$$\{r_{R_j}\} = \frac{2}{T} \int_{t_0}^{t_0+T} \{f\} \times \sin(\omega t) dt = \begin{bmatrix} f_{j1} \cos \theta_{j1} \\ f_{j2} \cos \theta_{j2} \\ \vdots \\ f_{jN} \cos \theta_{jN} \end{bmatrix} \quad (2.31)$$

$$\{r_{I_j}\} = \frac{2}{T} \int_{t_0}^{t_0+T} \{f\} \times \cos(\omega t) dt = - \begin{bmatrix} f_{j1} \sin \theta_{j1} \\ f_{j2} \sin \theta_{j2} \\ \vdots \\ f_{jN} \sin \theta_{jN} \end{bmatrix} \quad (2.32)$$

In the above equations T is one period of time. Polynomial curve fitting will be applied to the real and imaginary parts of $\{r_j\}$, $\{r_{R_j}\}$ and $\{r_{I_j}\}$.

$$[R] = [R_R] + i[R_I] \quad (2.33)$$

$$[R_R] = \sum_{p=0}^P c^p [T^p] \quad (2.34)$$

$$[R_I] = \sum_{p=0}^P c^p [Z^p] \quad (2.35)$$

Using Eqs. (2.34) and (2.35), the aerodynamic forces have been separated to real and complex parts and expressed in terms of a Pth order polynomial. The variable

c , which is the independent variable of the polynomial, can be taken as the oscillation frequency “ ω ” or reduced frequency k .

$$k = \frac{\omega b}{U_\infty} \quad (2.36)$$

where,

b : the half of the chord, sometimes taken at $3/4$ span

U_∞ : freestream speed

Denoting by $\{\bar{\eta}\}$, the real and imaginary parts of $\{\eta\}$

$$\{\bar{\eta}\} = \begin{bmatrix} \{\eta_R\} \\ \{\eta_I\} \end{bmatrix} \quad (2.37)$$

Now, Eq. (2.30) can be defined as an augmented real system, and the real and imaginary parts are separated by doubling the size of the system. Using polynomial curve fitting in k , the polynomial eigenvalue problem is expressed as

$$\left(\sum_{p=0}^P k^p \bar{Q}_p \right) \{\bar{\eta}\} = \{0\} \quad (2.38)$$

where

$$\bar{Q}_0 = \begin{bmatrix} [K_M] & [0] \\ [0] & [K_M] \end{bmatrix}, \quad \bar{Q}_2 = Q_2 - \left(\frac{U_\infty}{b} \right)^2 \begin{bmatrix} [M_M] & [0] \\ [0] & [M_M] \end{bmatrix} \quad (2.39)$$

$$\bar{Q}_p = Q_p \text{ for } p = 1, 3, 4, \dots P \text{ and } Q_p = \begin{bmatrix} -[\Phi]^T [T_p] & [\Phi]^T [Z_p] \\ -[\Phi]^T [Z_p] & -[\Phi]^T [Z_p] \end{bmatrix} \quad (2.40)$$

The eigenvalues of Eq. (2.38) are k 's (reduced frequency).

CHAPTER 3

MODAL ANALYSIS OF AGARD WING 445.6

3.1 Introduction

In this chapter, modal analysis of the AGARD Wing 445.6 will be performed in order to extract the modal parameters, the modal frequencies and mode shapes of the structure. The extracted data will be compared with the previous studies and experimental data. The modal data will be the inputs for the aerodynamic analysis which is discussed in the next chapter. The geometric and structural properties of the wing are given by Yates [9]. Using this information, the finite element model of the wing is created and the modal analysis is done with ANSYS® finite element software.

3.2 Finite Element Model

The finite element model of the wing is formed in accordance with the information given in [9]. The two dimensional drawing is given in Figure 3.1.

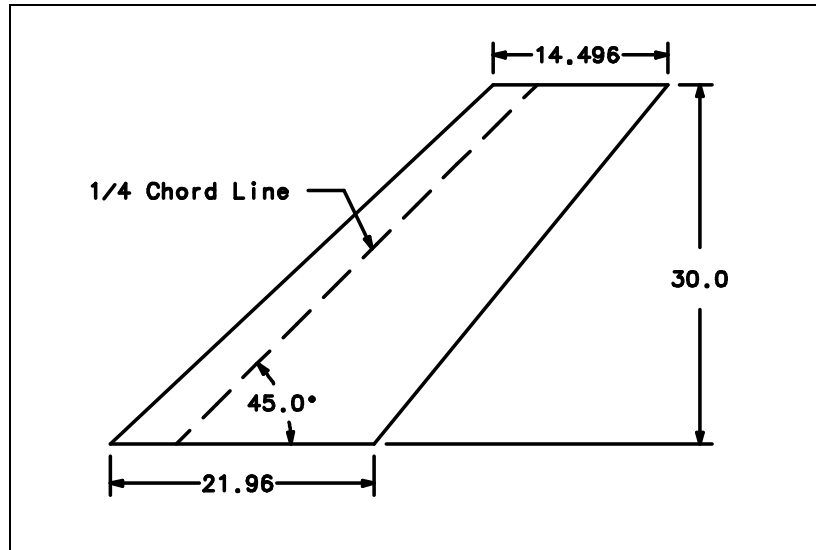


Figure 3.1 AGARD Wing 445.6

The structural model of the wing is made of shell elements. Hence, the wing model is not a box beam but a flat shell model of variable shell thickness. There are 10 elements in chordwise and 20 elements in spanwise direction. There are a total of 231 nodes and 200 elements. The material properties of the elements are given in Table 3.1. The thickness of each element is different and in accordance with the real wing thickness distribution as given in Figure 3.2. The macro file generated for ANSYS® solution is given in APPENDIX B. These files contain the complete finite element model of the wing.

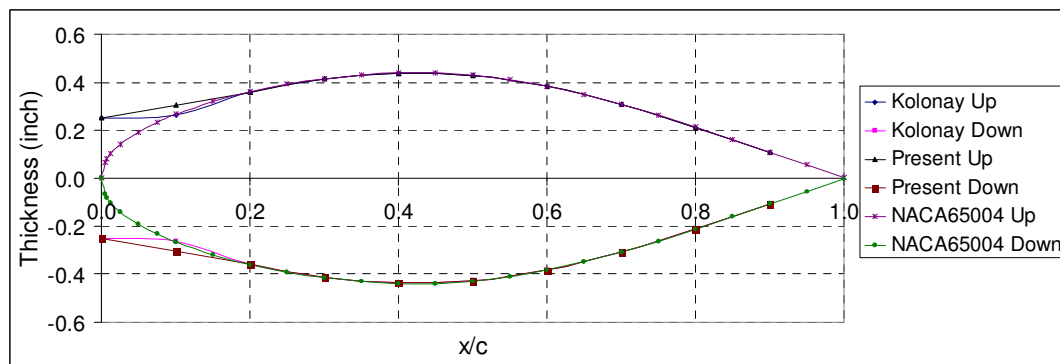


Figure 3.2. Airfoil Thickness Distribution

The thickness distribution of the finite element model coincides with the airfoil thickness distribution after 20% percent of the chord from the leading edge. However, the thickness distribution of the finite element model of Kolonay [10] coincides with the original thickness distribution after 10% of chord from the leading edge.

Table 3.1 Physical Properties of AGARD Wing 445.6

Property	Value
Density (slug/in ³)	35.2×10^{-6}
E _x (psi)	0.45072×10^6
E _y (psi)	0.060367×10^6
G (psi)	0.63700×10^6
Poisson's Ratio	0.04152

Modulus of elasticity in x-direction is defined to be along the grain of the wing which is parallel to the wing leading edge. Because of this, the material coordinate system of the elements is rotated such that x-axis is parallel to the wing leading edge. The structural damping is assumed to be non-existing for flutter analysis. The finite element model is shown in Figure 3.3.

The boundary conditions of the wing are selected in accordance with the physical model. The root is cantilevered except for the nodes at the leading and trailing edges. Additionally, the rotation around z-axis degree of freedom at all nodes is constrained to zero.

Using this finite element model the modal analysis of the structure is carried out. The discussion on the results of this analysis is given in the next section.

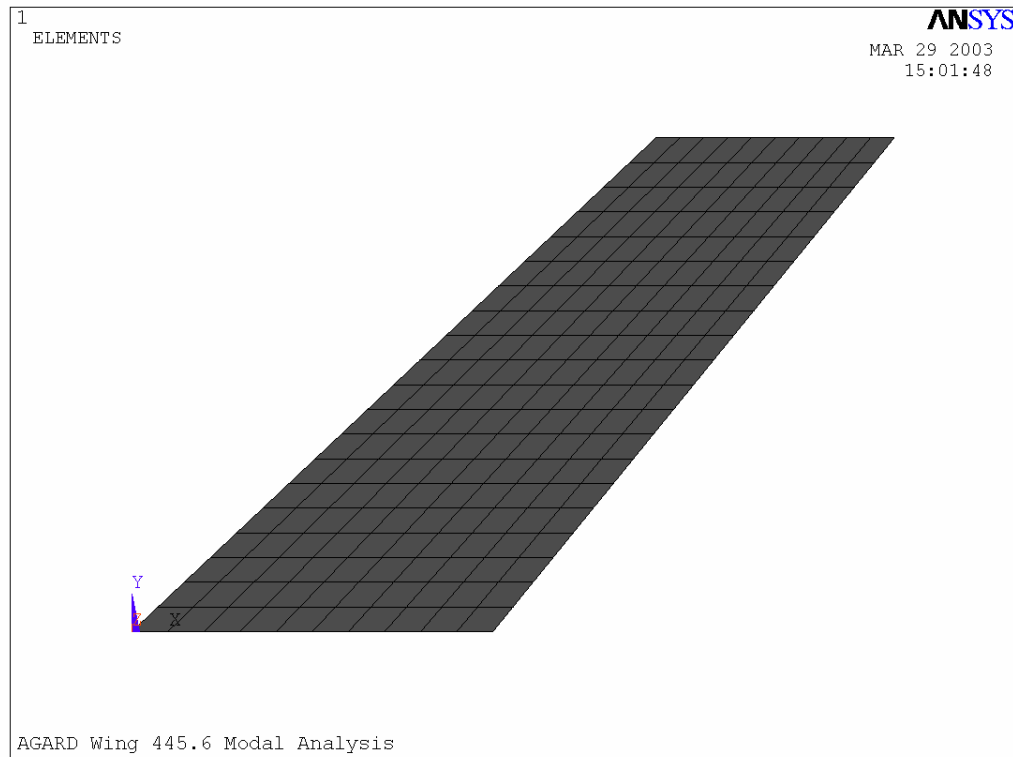


Figure 3.3 AGARD Wing 445.6 Finite Element Model

3.3 Modal Analysis

A modal analysis study covers calculation of natural frequencies and mode shapes of a structure. Natural frequency can be defined as the frequency at which free vibration of the system can take place and mode shape is the deflection of the points on the structure for that mode. Deflection values in the mode shape matrix are not absolute deflections; they should be either normalized to unity or normalized with respect to the mass matrix. Free vibration of a structure can be formulated as given in Eq. (3.1).

$$[M]\{\ddot{q}\} + [C]\{\dot{q}\} + [K]\{q\} = \{0\} \quad (3.1)$$

M is the mass matrix, K is the stiffness matrix and C is the damping matrix of the system. For undamped systems the damping matrix C equals to zero and Eq. (3.1) reduces to

$$[M]\{\ddot{q}\} + [K]\{q\} = \{0\} \quad (3.2)$$

Assuming harmonic free vibrations, the displacements can be defined as

$$\{q\} = \{u\} e^{i\omega t} \quad (3.3)$$

Substituting in Eq. (3.1)

$$-\omega^2 [M]\{u\} + [K]\{u\} = \{0\} \quad (3.4)$$

This equation is an eigenvalue problem, the eigenvalues are the squares of natural frequencies and the eigenvectors are the mode shapes.

The mode shapes and modal frequencies of the structure are calculated using the finite element model given in the previous section. The natural frequencies of the structure are given in Table 3.2 together with the experimental results and results of the previous studies.

As given in Table 3.2, calculated natural frequencies are in very good agreement with the experimental data. Calculated natural frequencies will be used as inputs to unsteady aerodynamic calculations.

The mode shapes of the structure are also calculated together with natural frequencies. Since the experimental mode shapes of the structure are not available

as quantitative comparable results, the comparison of the mode shapes will be made with the results of Kolonay [10].

Table 3.2 Natural Frequency Comparison

Natural Frequency (Hz)							
Modes	Experiment [9]	Present Study / %Error		Kolonay [10] / %Error		Li [11] / %Error	
1	9.60	9.688	0.92	9.63	0.31	10.85	13.02
2	38.10	37.854	-0.65	37.12	-2.57	44.57	16.98
3	50.70	50.998	0.59	50.50	-0.39	56.88	12.19
4	98.50	92.358	-6.24	89.94	-8.69	109.10	10.76

Comparison will be made by plots of mode shapes and maximum and minimum deflection values. The calculated mode shapes are normalized with respect to the mass matrix. In Table 3.3 the maximum and minimum deflection values are compared. These deflection values are the out-of-plane (vertical) deflection values of each mode shape of the wing, because, during the experimental studies of AGARD Wing 445.6, the amplitudes of oscillation were small enough so that the motion of the wing was dominated by only the out-of-plane displacements [9],[8].

The maximum and minimum values for the 2nd mode are in reverse order, that is there is 180 degrees of phase shift between them. This is due to the difference of solvers.

Table 3.3 Maximum / Minimum Deflection Comparison

Mode	Present Study		Kolonay [10]	
	Min	Max	Min	Max
1	-0.0125	28.093	-0.08551	27.92
2	-25.375	45.873	-45.48	25.09
3	-27.923	31.595	-27.17	31.38
4	-22.82	67.182	-22.62	71.52

It is observed from Table 3.3 that maximum difference of 6% occur at the fourth mode. The first mode shape of the structure is compared below.

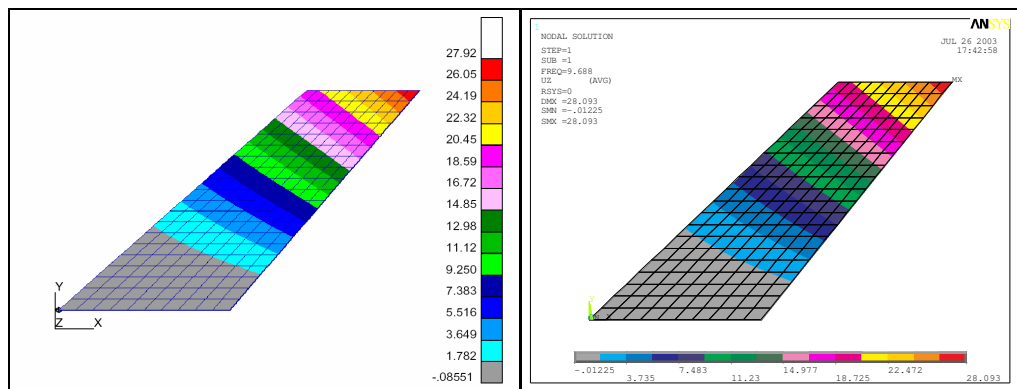


Figure 3.4 Kolonay, Mode 1

Figure 3.5 Present Study, Mode 1

The second mode shape of the structure is compared below.

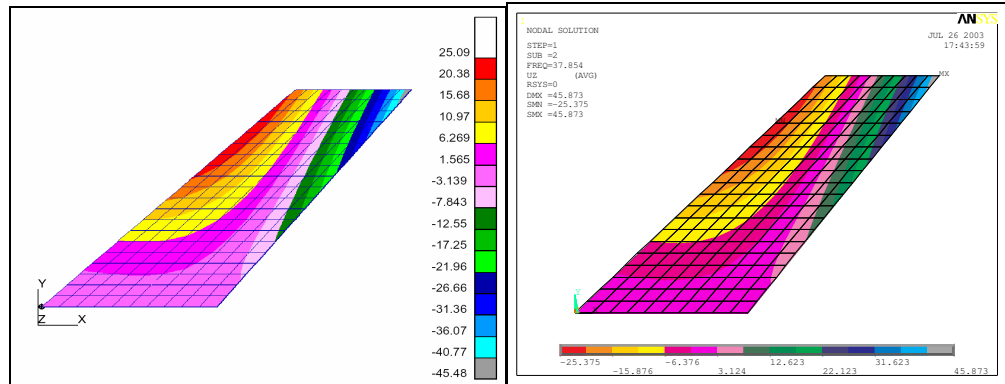


Figure 3.6 Kolonay, Mode 2

Figure 3.7 Present Study, Mode 2

The third mode shape of the structure is compared below.

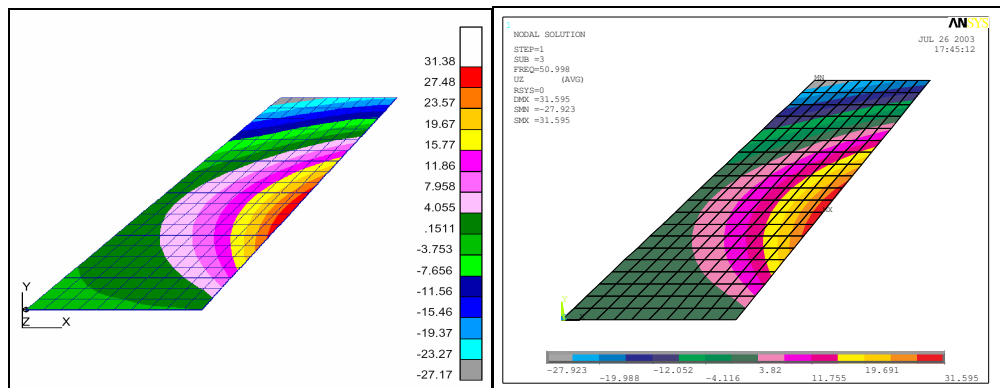


Figure 3.8 Kolonay, Mode 3

Figure 3.9 Present Study, Mode 3

The fourth mode shape of the structure is compared below.

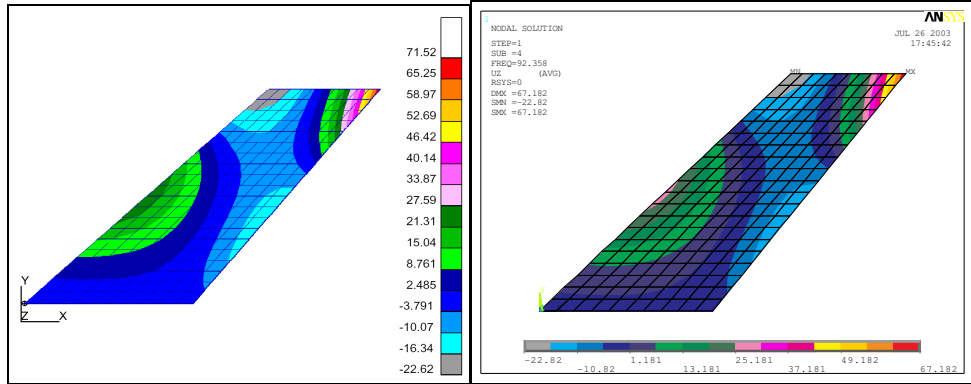


Figure 3.10 Kolonay, Mode 4

Figure 3.11 Present Study, Mode 4

The comparisons with the experimental results and previous studies have shown that the modal analysis results can be used in further analysis. In Figure 3.12, the mode shapes of the AGARD Wing 445.6 are given from [9].

The modal analysis of the AGARD Wing 445.6 has been carried out once more by constraining five degrees of freedom except the deflection in z-direction. However, as shown in Table 3.4 the natural frequencies calculated are much higher compared to experimental ones.

Table 3.4. Modal Analysis with 1 DOF in Z-Direction

Mode #	Frequency (Hz)
1	223.13
2	546.05
3	809.14
4	870.69

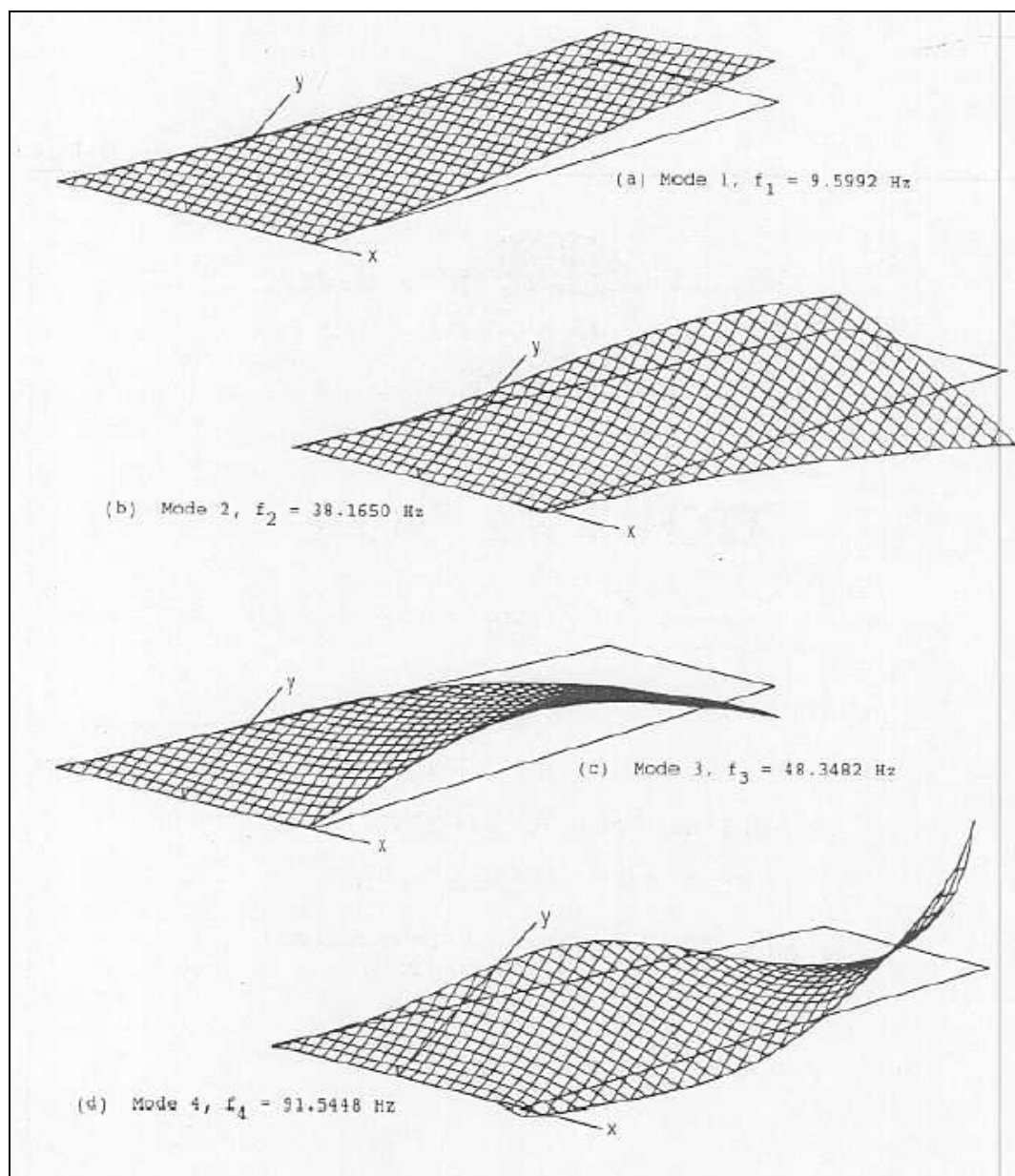


Figure 3.12. Mode Shapes of AGARD Wing 445.6

CHAPTER 4

AERODYNAMIC ANALYSIS OF AGARD WING 445.6

4.1 Introduction

The aerodynamic analysis of the AGARD Wing 445.6 is performed with a 3D Unstructured Euler Solver (USER3D) [12]. The unsteady loads caused by the harmonic oscillation of the wing are calculated. The solution domain is updated at each time step according to the deflection of the wing by the moving mesh algorithm [13]. Unsteady aerodynamic loads calculated on the CFD model are transformed to the structural model using a surface interpolation technique.

4.2 Theory of USER3D Computational Fluid Dynamics Solver

USER3D is a parallel finite-volume based unstructured Euler solver. The serial version of the program has been developed by Oktay [12], the parallel version of the program has been developed at CFD Laboratory of Indiana University – Purdue University Indianapolis (IUPUI) [13].

The program uses Arbitrary Lagrangian-Eulerian (ALE) formulation of the three dimensional inviscid flow equations in integral form given below

$$\frac{\partial}{\partial t} \iiint Q dV + \iint \vec{F} \cdot \vec{n} dS = 0 \quad (4.1)$$

rewriting in conservative form, Eq. (4.1) becomes

$$\frac{\partial Q}{\partial t} + \frac{\partial F}{\partial x} + \frac{\partial G}{\partial y} + \frac{\partial H}{\partial z} = 0 \quad (4.2)$$

In this formulation;

$$Q = [\rho \quad \rho u \quad \rho v \quad \rho w \quad e]^T \quad (4.3)$$

is the vector of conserved flow variables. Where

- ρ ; non-dimensional density
- ρu ; non-dimensional momentum in x-direction
- ρv ; non-dimensional momentum in y-direction
- ρw ; non-dimensional momentum in z-direction
- e ; non-dimensional energy

These variables are dimensionalised as given in Eq. (4.4)

$$\begin{aligned} \rho' &= \rho \cdot \rho_0 \\ u' &= u \cdot a_0 \\ v' &= v \cdot a_0 \\ w' &= w \cdot a_0 \\ a' &= a \cdot a_0 \\ T' &= T \cdot T_0 \\ P' &= P \cdot \rho_0 a_0^2 \quad P' = P \cdot P_0 \gamma \end{aligned} \quad (4.4)$$

$$\vec{F} = \left[(\vec{V} - \vec{W}) \cdot \vec{n} \right] \begin{bmatrix} \rho \\ \rho u \\ \rho v \\ \rho w \\ e + p \end{bmatrix} + p \begin{bmatrix} 0 \\ n_x \\ n_y \\ n_z \\ W_n \end{bmatrix} \quad (4.5)$$

In Eq. (4.3), we have pure Lagrangian formulation if $\vec{V} = \vec{0}$ and pure Eulerian if $\vec{W} = \vec{0}$

$$\vec{n} = n_x \vec{i} + n_y \vec{j} + n_z \vec{k} \quad (4.6)$$

$$\vec{V} = u \vec{i} + v \vec{j} + w \vec{k} \quad (4.7)$$

$$\vec{W} = \vec{i} \frac{\partial x}{\partial t} + \vec{j} \frac{\partial y}{\partial t} + \vec{k} \frac{\partial z}{\partial t} \quad (4.8)$$

$$W_n = \vec{W} \cdot \vec{n} = n_x \frac{\partial x}{\partial t} + n_y \frac{\partial y}{\partial t} + n_z \frac{\partial z}{\partial t} \quad (4.9)$$

Q : the vector of conserved flow variables.

\vec{F} : the convective flux tensor.

\vec{n} : the normal vector to the boundary.

\vec{V} : the fluid velocity.

\vec{W} : the mesh velocity.

W_n : the face speed of finite-volume cells.

The pressure “ p ” can be calculated from

$$p = (\gamma - 1) \left[e - \frac{1}{2} \rho (u^2 + v^2 + w^2) \right] \quad (4.10)$$

Characteristic boundary conditions are applied on the farfield using Riemann invariants. Cell-centered finite volume formulation is employed in USER3D with implicit time integration scheme [13].

$$\{\Delta Q\}^n \frac{V^{n+1}}{\Delta t} = - \iint_{\partial\Omega} \vec{F}(Q) \cdot \vec{n} dS - \{Q\}^n \frac{\Delta V^n}{\Delta t} \quad (4.11)$$

Here, $\Delta Q^n = Q^{n+1} - Q^n$ and $\Delta V^n = V^{n+1} - V^n$ is the increment in volume at one time step. According to the implicit time-integration formulation, fluxes are calculated at time step $n+1$.

$$R^{n+1} = R^n + \frac{\partial R^n}{\partial Q^n} \Delta Q^n \quad (4.12)$$

therefore, the following equations should be solved at each time step of solution.

$$[A]^n \{\Delta Q\}^n = \{R\}^n - \{Q\}^n \frac{\Delta V^n}{\Delta t} \quad (4.13)$$

where

$$[A]^n = \frac{V^n}{\Delta t} [I] - \frac{\{\partial R\}^n}{\{\partial Q\}^n} \quad (4.14)$$

$$\{R\}^n = - \iint_{\partial\Omega} \vec{F}(Q)^n \cdot \vec{n} dS \quad (4.15)$$

The flow variables are calculated at the center of each tetrahedron and flux quantities are calculated using Van Leer's flux vector splitting or Roe's flux difference splitting method [13].

4.3 Moving Mesh Algorithm

USER3D utilizes a moving mesh algorithm [13] for aeroelastic analysis. At each time step of solution, the elastic body movement is reflected to the solution domain. The whole volume grid is deformed accordingly through a spring analogy.

The spring method assumes that the nodes of a tetrahedral element are connected by a spring as shown in Figure 4.1 and the stiffness of the spring is inversely proportional to the distance between nodes.

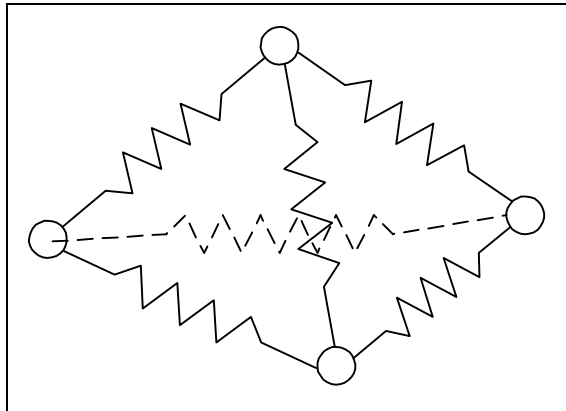


Figure 4.1 Tetrahedral Element

The stiffness between each node is calculated from

$$k_m = \sqrt{\left(x_j - x_i\right)^2 + \left(y_j - y_i\right)^2 + \left(z_j - z_i\right)^2} \quad (4.16)$$

The nodes at the outermost boundary are fixed, however the locations of the nodes on the moving body are calculated at each time step according to the body motion. After all nodes in the interior volume are relocated, the cell and face velocities of each element are calculated.

The computational fluid dynamics solver USER3D implements the geometric conservation law as

$$\frac{\partial}{\partial t} \iiint_{\Omega} dV = \iint_{\partial\Omega} \vec{W}_s \cdot \vec{n} dS \quad (4.17)$$

which is obtained by setting $\rho=1$ in the mass conservation law. The volume of each cell can be calculated from

$$V_i^{n+1} = V_i^n + \Delta t \sum (x_{t_m}^{n+1} A_x + y_{t_m}^{n+1} A_y + z_{t_m}^{n+1} A_z) \quad (4.18)$$

where A 's are the projections of the lateral surface areas onto the cartesian planes. The geometric conservation law has to be solved in each time step because the moving mesh algorithm may cause a violation of mass, energy and/or momentum conservation. Geometric conservation law is solved together with mass, momentum and energy conservation laws.

4.4 Computational Fluid Dynamics Model

For the CFD solution of the AGARD Wing 445.6, unstructured volume grid is generated using I-DEAS® 3D modeling software. An unstructured grid is composed of tetrahedral elements. The surfaces of the tetrahedral elements are triangles whereas a structured grid is composed of rectangular elements and solution is carried out on an orthogonal grid coordinate system.

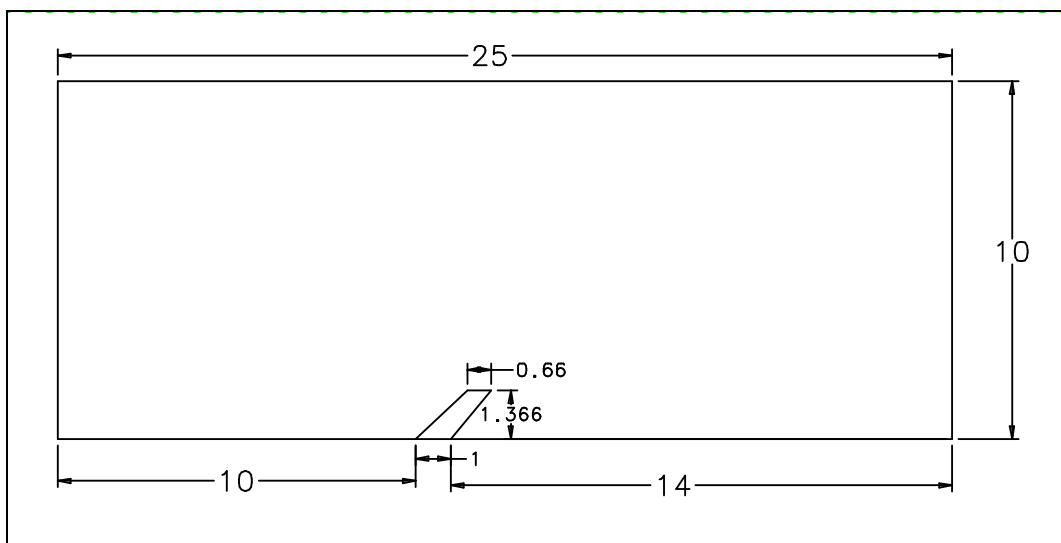


Figure 4.2 Relative Size of the Solution Domain

The volume grid generated for the CFD solution is non-dimensionalised with respect to the root chord length of the wing (21.96"). The relative dimensions of the volume are shown in Figure 4.2. The profile of the AGARD Wing 445.6 is NACA65A004 airfoil. The volume grid has been generated for half of the solution domain as shown in Figure 4.3 that is for the region on one side of the wing symmetry plane. The full domain grid is obtained by mirroring the half and then joining two half volumes. The solution is carried out in the full domain since the problem is not symmetric with respect to wing symmetry plane. The full volume

grid is shown in Figure 4.4. The wing symmetry plane is located in xy plane in the figures.

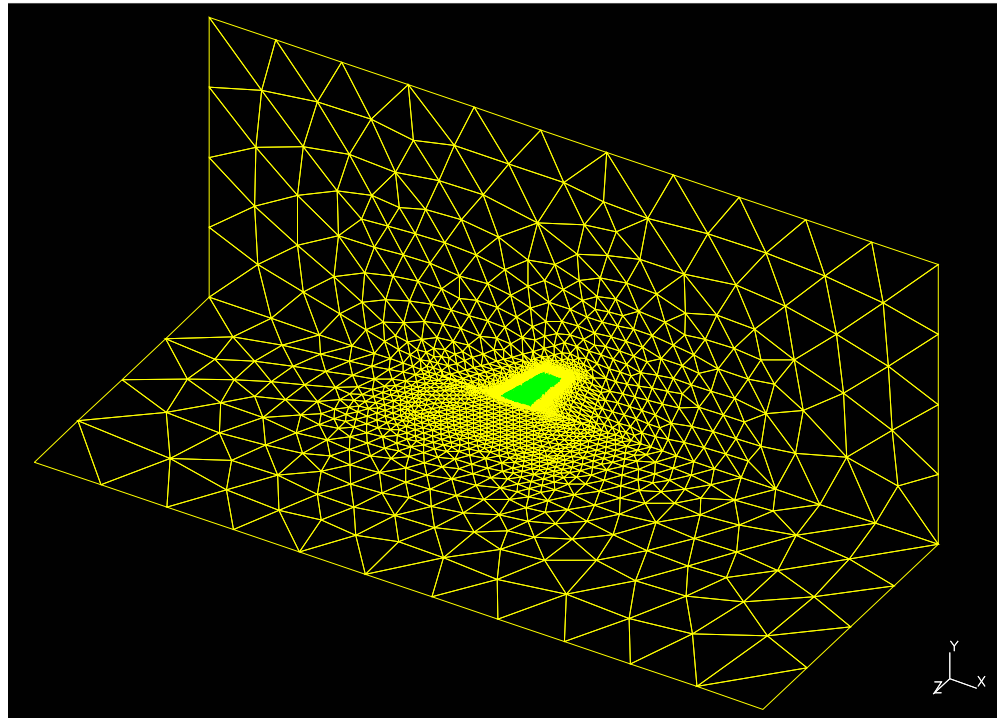


Figure 4.3 Unstructured Volume Grid (Half)

There are a total of 126380 elements and 26027 nodes in the single domain grid. The elements are refined on the wing surface to obtain an accurate solution. There exist four interior control regions to adjust the element size distribution in the volume. The global element size definition is defined in increasing order from the most inner one to the most outer region. The non-dimensional surface mesh on the wing is shown in Figure 4.5. It can be observed that the element size increases away from the leading and trailing edges of the wing and decreases toward the edges. The control of element size distribution on the wing surface is maintained by using the free mapped mesh definition in I-DEAS[®]. This type of mesh

definition has the advantages of the local element length control algorithms for structured meshes, which is applied to an unstructured mesh.

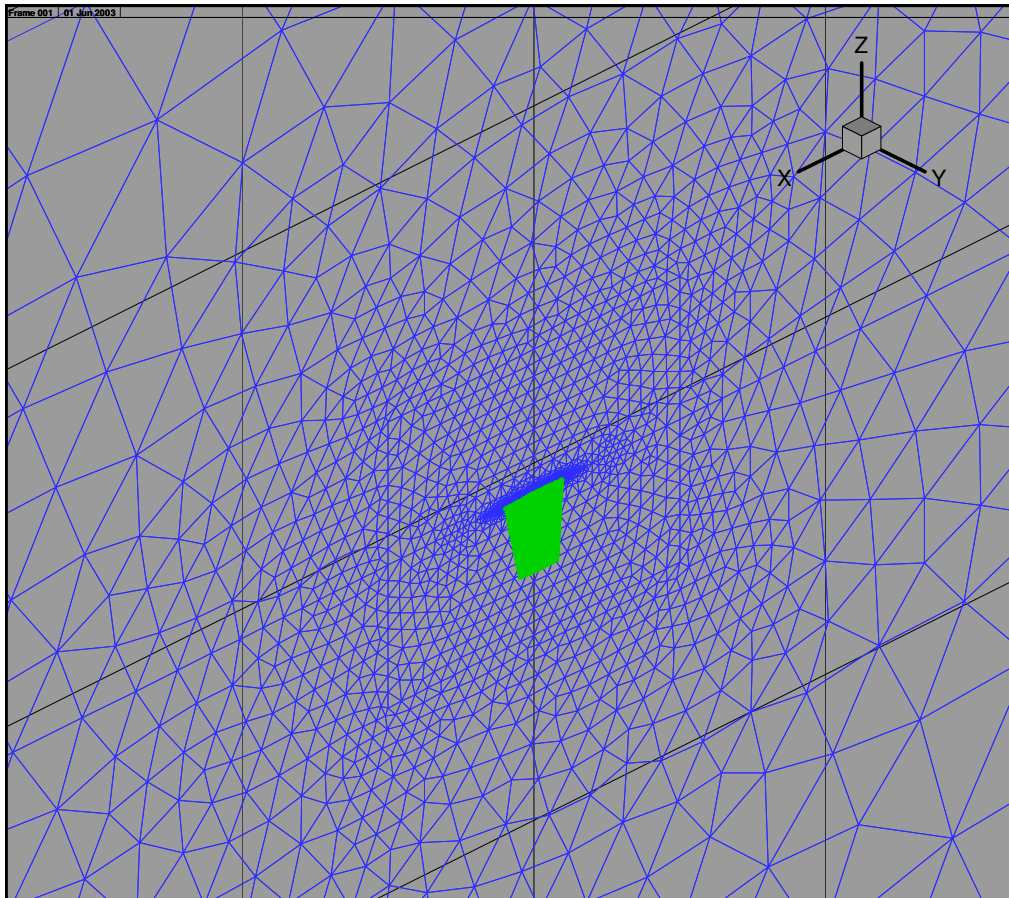


Figure 4.4 Unstructured Volume Grid (Full)

There are a total of 13254 elements and 6667 nodes on the wing surface for the single block grid which is shown in Figure 4.5.

In order to solve the domain in a parallel processing environment, the grid has been divided into 8 blocks. After division, number of elements and nodes for each block is given in Table 4.1.

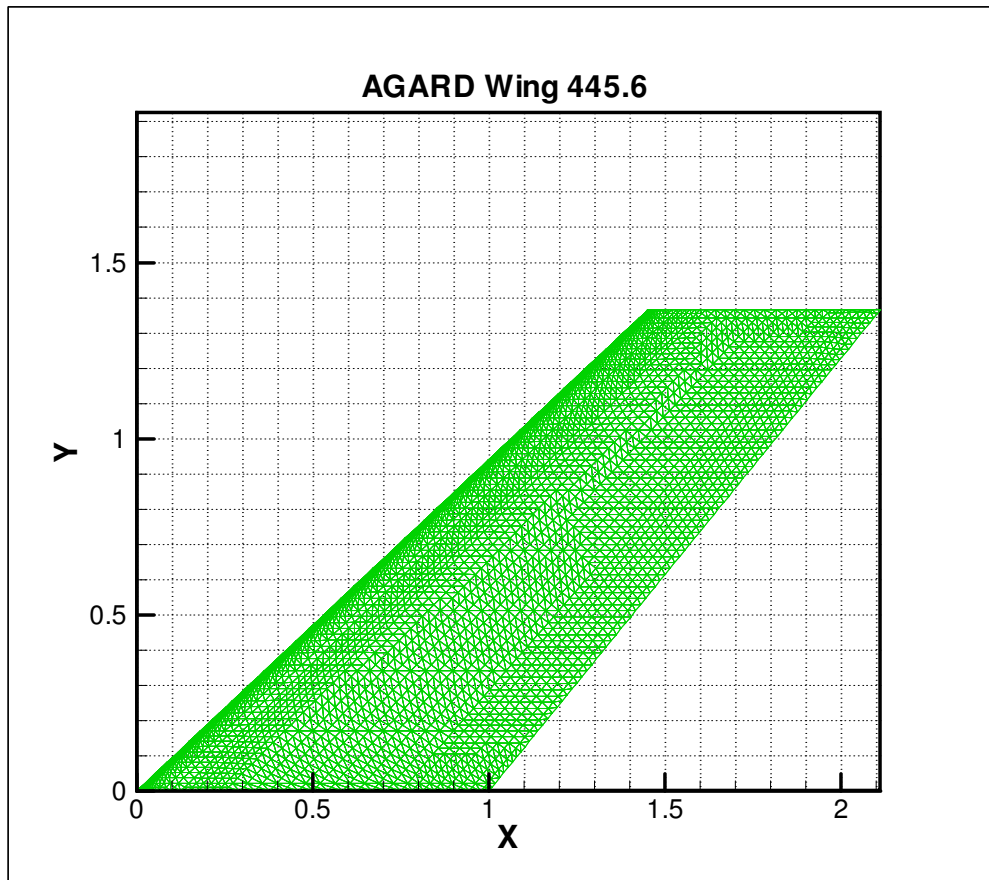


Figure 4.5 Wing Surface Mesh

MPI (Message Passing Interface) is used in USER3D to construct parallelization. “MPI is a message-passing application programmer interface, together with protocol and semantic specifications for how its features must behave in any implementation. MPI includes point-to-point message passing and collective (global) operations, all scoped to a user-specified group of processes.” [17]. Particularly, MPICH library [17], which is a portable and high performance implementation of MPI, is used in USER3D.

Each block is solved by a separate processor, and at the end of each time step of solution, every block transfers the flow field information to the others. Therefore, at time step t each block uses the flow field information of neighboring elements

calculated at time step $t-1$. As it can be observed from Table 4.1 number of nodes and elements are close to each other since all processes must solve the same time step together and all must wait for the others to finish. In addition, the total number of nodes and elements are more than that of the single domain grid since interface elements between blocks appear twice, that is, once in each adjacent block.

Table 4.1 Node / Element Information for each Block

Block #	# of Nodes	# of Elements
1	3638	16847
2	3764	18548
3	3801	17298
4	3825	16678
5	3920	16571
6	3882	18266
7	3878	17107
8	3560	15349
Total	30268	136664

For the unsteady solution in USER3D, first, the steady flow around the wing is calculated, and then starting from this initial condition, unsteady loads are calculated at each time step.

The necessary modifications of USER3D are done at the ROKETSAN Missile Industries Inc parallel computing facility and the solutions are done at the eight-node parallel computing environment in the Department of Aerospace Engineering [18]. Each node is a dual PIII 700 MHz processor workstation machine with 512 MB RAM. The operating system of each node is Linux with Kernel version 2.2.

4.5 Solution Procedure

The present solution procedure is quite different from a coupled CFD-CSD (Computational Structural Dynamics) solution which is previously calculated by USER3D [14], however at each time step of solution the deformation of the grid is not calculated by the CSD solver, but a sinusoidal oscillation for each mode shape is prescribed into USER3D. The solution procedure is shown in Figure 4.6.

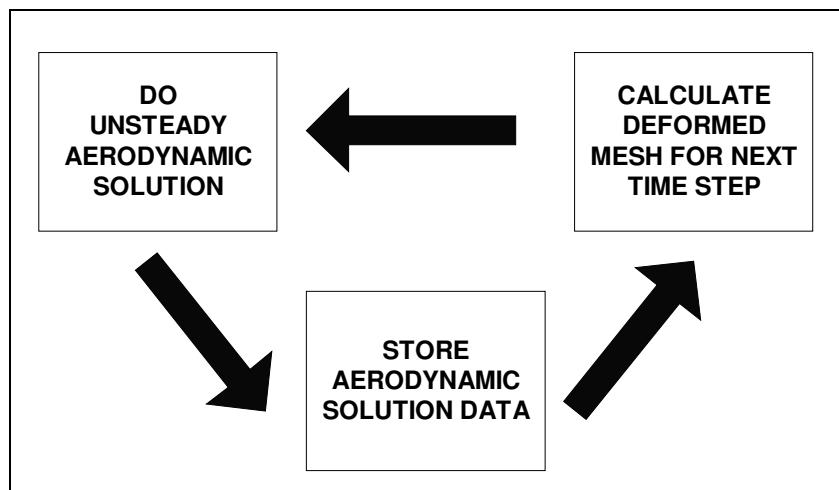


Figure 4.6. Modified Solution Procedure

The deformed mesh for each time step is calculated according to the mode shapes of the structure. The mode shapes of the structure which are calculated with ANSYS, are normalized with respect to unity. On the other hand, the maximum deflections used for each mode shape in CFD solution are given in Table 4.2. They are based on the calculations of Kolonay [10]. The maximum tip deflections are non-dimensionalised with respect to the root chord length (c) of the wing.

Table 4.2. Maximum Tip Deflections Input to the CFD Code for Each Mode

Mode #	Maximum Tip Deflection (inch)
1	0.015
2	0.03
3	0.004
4	0.0015

The sinusoidal oscillation of a structure according to the mode shape is formulated as

$$\{Q\} = \{Q_0\} \times \sin(\omega t) \quad (4.19)$$

in this formulation,

ω : frequency of oscillation (1/s)

t : absolute time (s)

The location of each node on the wing at time t is calculated according to Eq (4.19). The stored aerodynamic data is later utilized to find the aerodynamic loading on the wing. The runs have been carried out at 40 different input conditions. These conditions vary according to mode shape, oscillation frequency, and time step of solution. The input conditions are chosen according to the approach proposed by Akgün [16]. In this thesis, first four modes of the structure were taken into consideration although first two modes are usually enough for

flutter prediction [1]. Unsteady load calculation at each mode shape was carried out at six more frequencies in addition to the four natural frequencies associated with the mode shapes. These frequencies are listed in Table 4.3. The calculations are carried out at 0.678 Mach and 0° angle of attack.

Table 4.3. Frequencies Used for Aerodynamic Solution for Each Mode Shape

Frequency No	Run Code	Frequency (Hz)	Δt (non-dim)
1	runM1X	9.688	0.524321
2	runM11X	19.077	0.266274
3	runM12X	28.465	0.178449
4	runM2X	37.854	0.134189
5	runM21X	44.426	0.114339
6	runM3X	50.998	0.099604
7	runM31X	61.338	0.082814
8	runM32X	71.678	0.070867
9	runM33X	82.018	0.061933
10	runM4X	92.358	0.054999

The listed time step values are non-dimensionalised with c/a (*chord length (m) / speed of sound (m/s)*). Using these time steps, one period of oscillation corresponds to 120 time steps. Each solution is carried out for 360 time steps, that is, for three periods of oscillation. In order to judge that this time step is appropriate for solution, two of the cases have been run with the above given time steps, and with one tenth of the above given time steps. These two cases are the first mode shape oscillating at its own natural frequency, and the first mode shape oscillating at the fourth natural frequency. The details of this study are explained in section 4.7.

As given in Chapter 2, frequencies 1, 4, 6, 10 correspond to the natural frequencies of the AGARD Wing 445.6. Since a polynomial curve fitting will be applied to the calculated aerodynamic forces at each node, ten frequencies covering the frequency range of four modes have been selected for calculations. The Run Code column given in Table 4.3 lists the names given to each case. The X stands for the mode shape number varying from 1 to 4.

4.6 Grid Transformation Between CFD and Solid Models

As shown in section 3.2, the structural finite element model of the wing is two-dimensional and consists of 231 nodes and 200 elements, whereas the computational fluid dynamics model of the wing consists of 6667 nodes and 13254 elements. The geometry transformation between the two models is done through a surface interpolation program (MODEINTERP) developed in this study.

MODEINTERP is used to interpolate the mode shape calculated with ANSYS over the three-dimensional wing body. The program takes the mode shape in the form of x, y, z coordinates of each structural node (totally 231) and calculates the z-coordinate of each node in the CFD wing surface mesh (totally 6667). The core of the MODEINTERP program is the surface interpolation routine which has been chosen from among IMSL FORTRAN routines. The DSURF (double precision) surface interpolation routine developed by Akima [15] is used in MODEINTERP. This routine is developed as a smooth surface fitting for irregularly distributed data points. The algorithm simply takes the original surface data in the form of $z(x,y)$ and outputs $z(x_i,y_i)$ for a given pair (x_i,y_i) .

Since the accuracy of an interpolation routine can not be guaranteed for every surface, the selected routine was tested with the mode shapes of the AGARD Wing 445.6. The verification is done for the first four mode shapes of the structure. The structural finite element model has 231 nodes distributed homogeneously, 11 nodes in the chordwise direction and 21 nodes in the spanwise direction. For each

mode shape, the surface is defined by 231 structural nodes. Using the surface interpolation, deflections of the same 231 nodes have been calculated. The percent error between the original deflection values and interpolated values are shown in Figure 4.7.

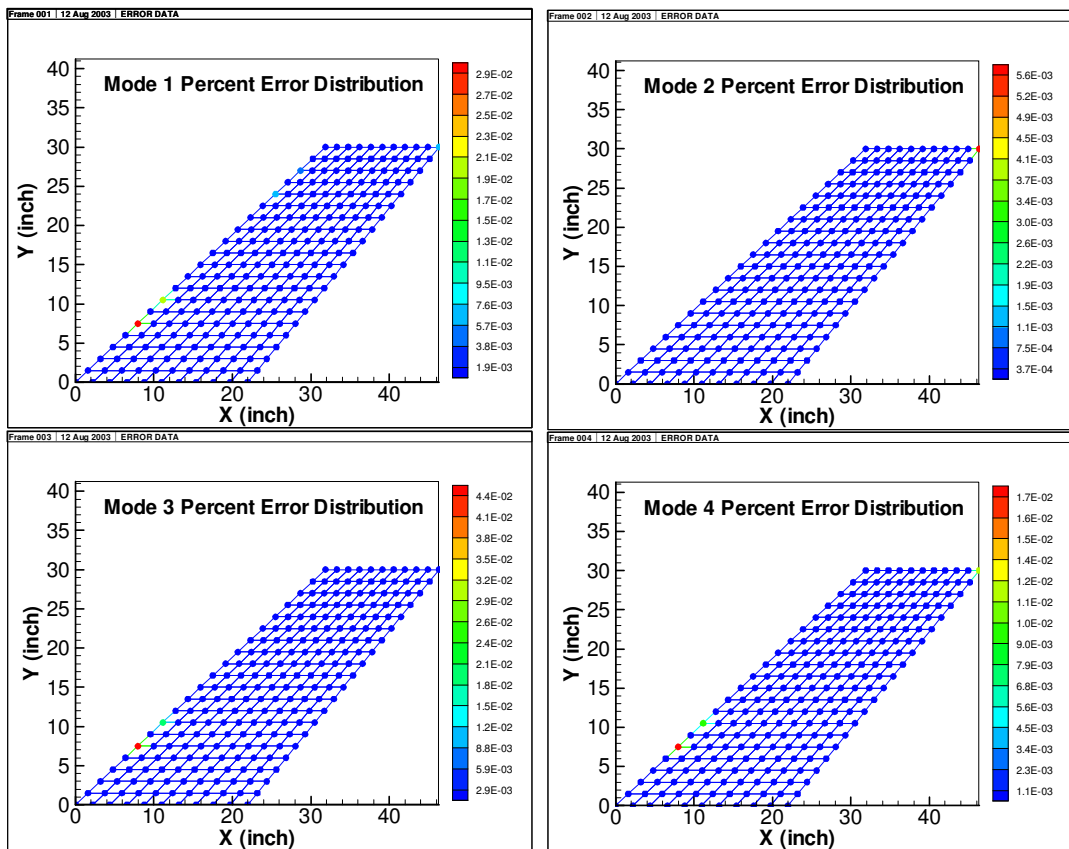


Figure 4.7 Percent Error Distribution for the Mode Shapes

As shown in Figure 4.7, the maximum percent of error is $4.4 \times 10^{-2} \%$ in the 3rd mode. Although the results of interpolation for all data points were expected to be coincident with the original points, there exist slight differences. These differences are assumed to be due to numerical accuracy problems and surface steepness at the points of consideration. It can be seen from the figure that the maximum errors for modes 1, 3, 4 are exactly at the same nodes (6th and 8th). Since the mode shapes at

that area are not too complex, it is thought that, the reason for the error at these locations is the numerical accuracy problem. For the second mode, the maximum error occurs at the tip point of the trailing edge, which is the maximum deflection point for that mode. For this reason, the error at this point is thought to be due to surface properties. For the fourth mode shape, the node at the tip of the trailing edge has a higher error compared to the other nodes on the wing similar to the second mode shape. The reason for this error is to be the same as for the second mode, since; again, that node is the maximum deflection point for the 4th mode shape.

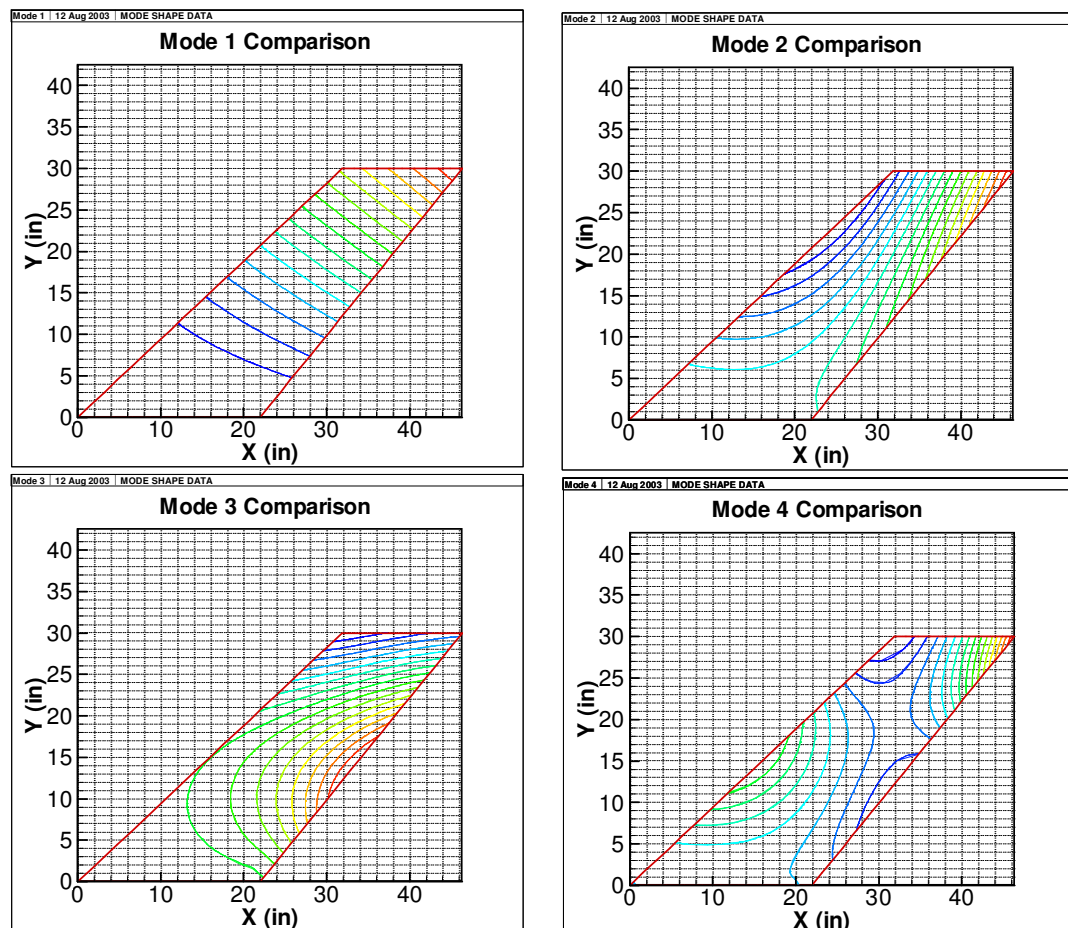


Figure 4.8 Comparison of the Mode Shapes between Structural and CFD Meshes

The interpolated mode shapes seem to be in good agreement with the original mode shapes and, therefore, the DSURF interpolation routine was chosen to be the surface interpolation function for the MODEINTERP program. As the last step of verification, the MODEINTERP program was applied to the original solution grid. In Figure 4.8, the original mode shape contours from the structural finite element model and the interpolated CFD surface mesh are drawn together for each mode. As seen from the figure, it is clear that, both the original contours and the interpolated contours are in good agreement.

The maximum difference between the original and the interpolated shapes arise in the fourth mode which has the most complex surface shape. The maximum distance between two points on the wing surface with same magnitude of z-deflection is around 0.2 inches (1% chord). Since this much difference occurs locally in a very small region, the MODEINTERP program is judged to be verified for the interpolation of the first four mode shapes of the AGARD Wing 445.6.

4.7 CFD Solution Results

The forty cases described above were solved with USER3D in the Department of Aerospace Engineering at METU. Solution of each case takes about 40-45 wall clock minutes. USER3D outputs the total lift coefficient (C_L), drag coefficient (C_D) and moment coefficient (C_M) at each time step. These coefficients help to judge the convergence of the solution to a steady-state oscillation. Additionally, the Euler variables given in Eq. (4.3) at each node of the solution domain are output at a selected number of time step intervals.

$$Q = [\rho \quad \rho u \quad \rho v \quad \rho w \quad e]^T$$

The pressure distribution in the domain is calculated using Eq. (4.10). The governing equations are non-dimensionalised as given in Eq. (4.4). The pressure distribution on the wing surface is transformed to structural nodes as forces using surface interpolation.

In order to decide about the number of time steps for each period, the first mode shape was solved at its own natural frequency and at the fourth natural frequency, both with 120 and 1200 time steps per period. In Figure 4.9, C_L variation with tip-deflection for the first mode shape at the first natural frequency with 120 and 1200 time steps is given. The “tip deflection” is the sinusoidal motion of wing tip in time. Since the solution is carried out for three periods of oscillation, the repeating behavior of C_L curve results in the given shape. It can be observed that, both of the solutions converge in time and the maximum difference between the two solutions is about 2.5×10^{-6} . In Figure 4.10, it can be observed that after the first peak, C_L settles to the oscillation frequency of 120 steps per period. A quantitative comparison among six peak values for 120 iterations can be made from Table 4.4 to verify convergence to steady oscillation.

Table 4.4. Maximum and Minimum Peak Values

Time Step #	C_L
488	0.000637
548	-0.000636
608	0.000636
668	-0.000636
728	0.000637
788	-0.000635

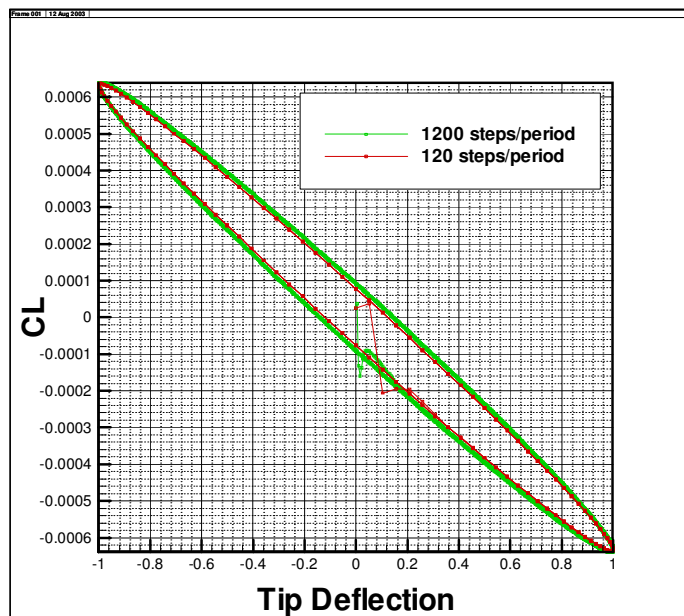


Figure 4.9. Variation of C_L with tip-deflection, the 1st mode shape at the 1st modal frequency

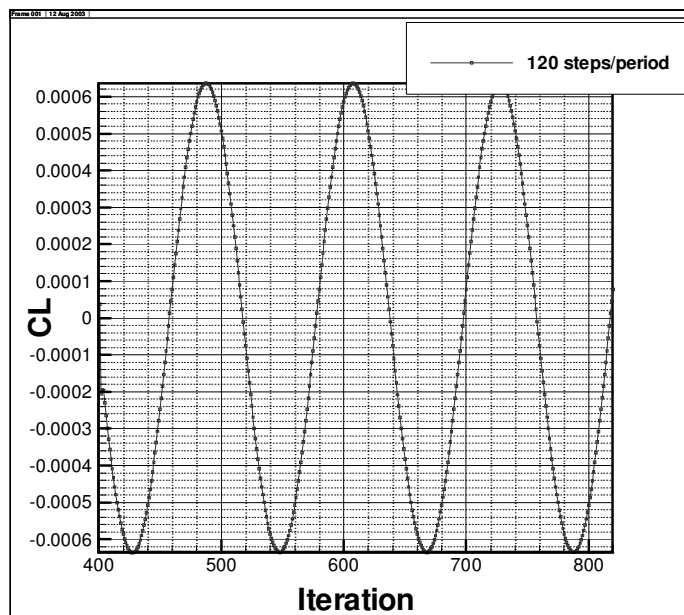


Figure 4.10. Variation of C_L with iteration, the 1st mode shape at the 1st modal frequency

It is seen from Table 4.4 that, the variation between peak values is 1×10^{-6} at most. Also the same small difference exists between maximum and minimum peak locations. Since the difference does not decrease in time and it is too small, it is judged to be due to numerical error.

Having obtained these results, it is judged that 120 steps per period can be used for the first natural frequency which is the lowest frequency among the solution cases. Next, first mode shape at the fourth natural frequency was investigated. Since the fourth natural frequency is the highest among the solution cases, it is much more likely to need smaller time steps. The number of time steps per period was kept the same as the first frequency, which meant smaller time steps. As it can be seen from Figure 4.11 there is no convergence problem for this case either.

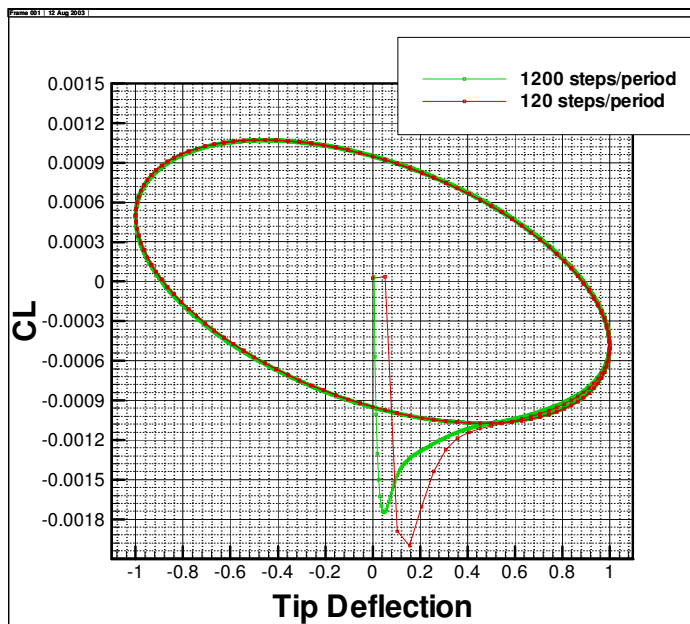


Figure 4.11 Variation of C_L with tip-deflection, the 1st mode shape at the 4th modal frequency

As a result of the above discussion, it is clear that using 120 time steps per period of oscillation is accurate enough for all of the forty solution cases. In Appendix A,

the C_L variations with deflection are given for the four modes at their corresponding natural frequencies for future reference.

In order to verify the CFD solution obtained, the variation of C_L between four modes is investigated. As given in Table 4.2, the maximum tip deflection occurs at the second mode. In addition, it can be observed from Figure 4.13 and Figure 4.14 that the maximum angle of attack occurs for the second mode also. Therefore, the second mode is expected to give the maximum total lift. Next, considering the mode shape and the tip deflection, the first mode is expected to give the second largest total lift coefficient. These can be observed from Figure 4.12.

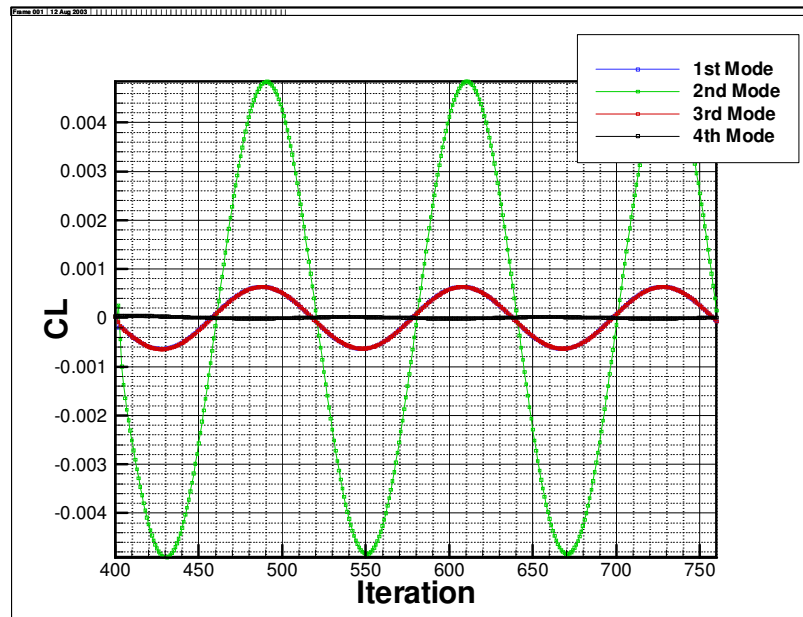


Figure 4.12. C_L comparison between four modes

It is seen that, the maximum value of the total lift coefficient C_L for the 2nd mode is much higher than the others as expected. However, C_L curves for the 3rd and 1st modes almost coincide such that the maximum difference between the two, at the peak points, is about 5.5×10^{-6} . This behavior is thought to be due to the elastic

angle of attack of the wing. In Figure 4.13, the sectional elastic angle of attack (AOA) values in spanwise direction are compared. These are defined as the angle between the horizontal and line passing through leading and trailing edge points of each spanwise section. Although the 3rd and 1st mode shapes of the wing are quite different, it can be seen from Figure 4.13 that, up to the half span of the wing, the sectional AOA of the wing at the 3rd mode shape is considerably higher than that of the 1st mode shape. This behavior is reversed for the other half and is more pronounced. However, because of the chord length decreasing in the spanwise direction, it becomes less effective on the total lift coefficient so that the two C_L values become almost equal.

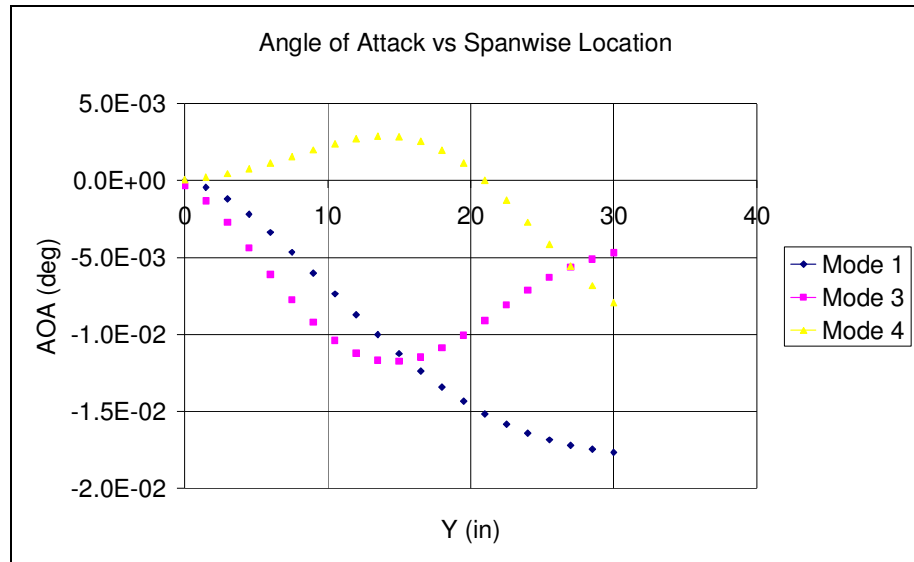


Figure 4.13. AOA Variation for 1st, 3rd and 4th modes

In addition, it is seen from Figure 4.12 that although the oscillation of the wing goes to the positive side, initially C_L values go to the negative side as the oscillation starts. This behavior is also explained by the AOA curves given in Figure 4.13 and Figure 4.14.

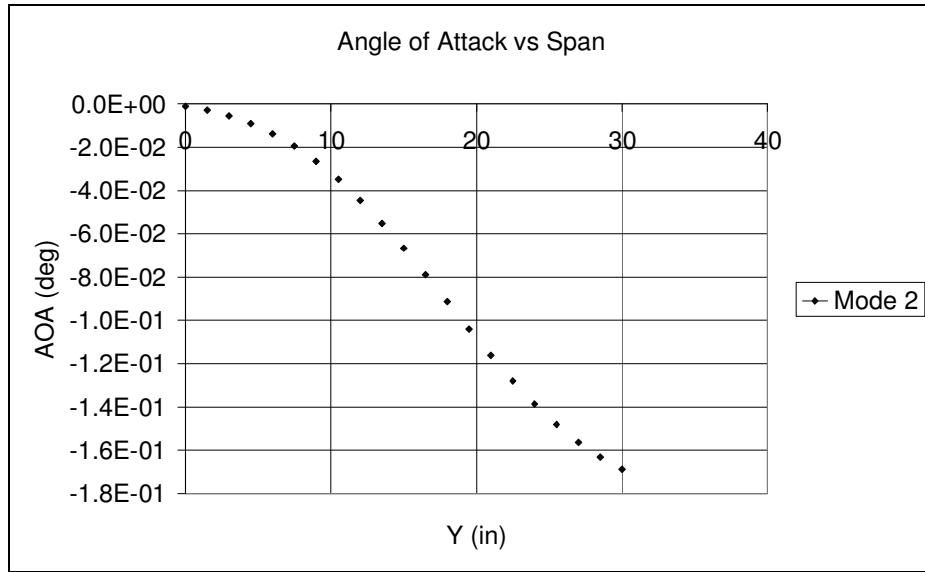


Figure 4.14. AOA Variation for the 2nd mode

The positive convention for the AOA is defined as the leading edge up. Therefore, it is clear that as the whole wing goes up, the trailing edge goes higher than the leading edge, this causes C_L to have the opposite sign of the direction of motion.

It can be observed from Figure 4.13 that the AOA values in spanwise direction for the fourth mode are very small and the sectional AOA changes sign in the spanwise direction since the mode shape is complex. This situation can be explained as the negative lift from the tip part of the wing canceling the positive lift from the root part, giving a very small total C_L as seen in Figure 4.12. In Figure 4.15, the C_L variation alone is given for the fourth mode. It is observed that since the resulting total lift coefficient values are very small, numerical errors become significant and affect the C_L curve.

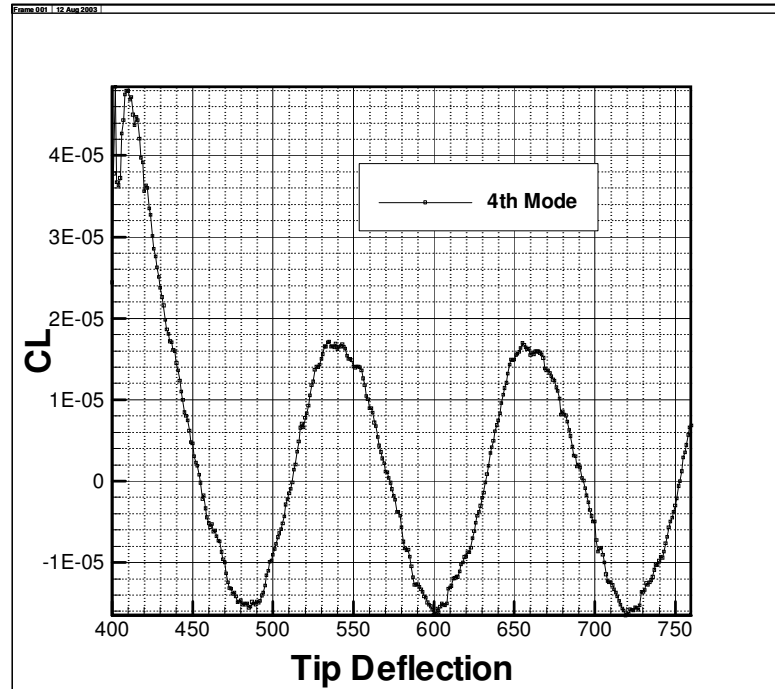


Figure 4.15. Variation of C_L for the 4th Mode

Next, in order to verify correctness of the aerodynamic results, some simple algorithms have been used to calculate the total C_L of the wing. Three different algorithms were used. The first method used is the simplest thin airfoil theory [20]. The next level of verification for the NACA65A004 airfoil is made with a panel code written by Kaya [21] at Aerospace Engineering Department of Middle East Technical University. The last verification method used is based on the 3D Vortex Lattice Method [22]. A program developed at the School of Aerospace, Mechanical and Mechatronic Engineering in University of Sydney has been used for the Vortex Lattice Method. In order to compare the results obtained, the first mode shape was used. The tip deflection of the wing was prescribed such that the sectional AOA at the tip would be 2° . This condition is assumed to be representing roughly an overall AOA of 1° for the wing. The sectional AOA distribution for this case is given in Figure 4.16.

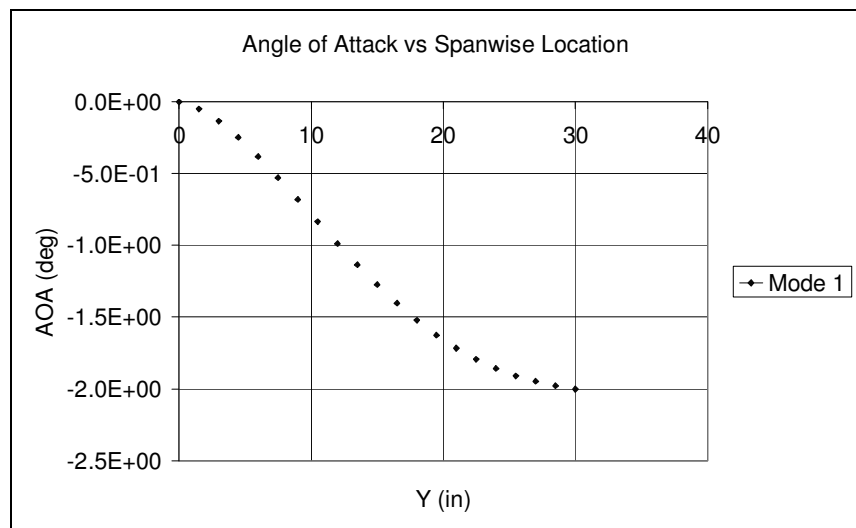


Figure 4.16. AOA variation for C_L verification, the 1st mode shape

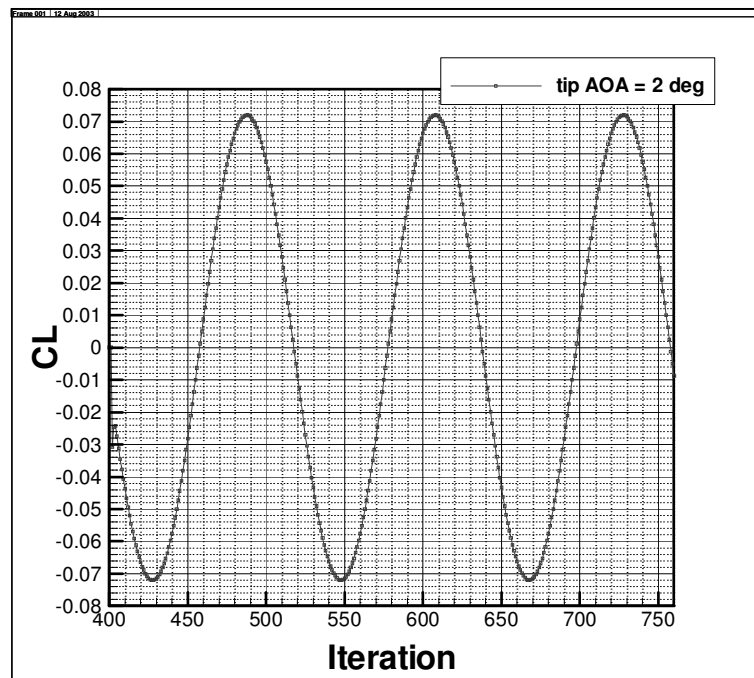


Figure 4.17. Variation of C_L with Iteration, the 1st mode at 2° AOA

The resulting total C_L curve has a maximum value of about 0.072 as shown in Figure 4.17. The figure is generated at the first modal frequency. The above result will be compared with the results of simple algorithms. Since these algorithms are all for steady flows, the results obtained from these methods will be evaluated considering this approximation. Generally, the peak unsteady lift coefficient around a wing is expected to be higher than the steady coefficient. The section of the AGARD Wing 445.6 is NACA65A004. The NACA65A004 airfoil has a maximum thickness of 2% of the chord length and it is symmetrical. The lift curve slope derived from simple thin airfoil theory for symmetric airfoils is

$$\frac{\partial C_L}{\partial \alpha} = 2\pi \quad (4.19)$$

Using the above equation, lift coefficient for the NACA65A004 airfoil at 1° of AOA is

$$C_L = 0.1097$$

This result is a very crude approximation for the steady flow around the AGARD Wing 445.6. Considering the three dimensional effects, the above calculated lift coefficient is very high compared to the actual case. In order to get a better approximation, the following equation which assumes a moderate to high aspect ratio wing with an elliptical lift distribution can be used.

$$\frac{\partial C_L}{\partial \alpha} = \frac{2\pi}{1 + (2/AR)(1 + \tau)} \quad (4.20)$$

where

AR is the aspect ratio of the wing

τ is a constant (usually $0.05 < \tau < 0.25$)

Using Eq. (4.20) with $\tau = 0$ which will give a higher C_L than actual, we get

$$C_L = 0.0682$$

The next verification was done with the two dimensional panel method solver [21]. Again, this method assumes an infinite span wing with given root airfoil, and expected to give much higher result compared to the actual steady flow around the three dimensional wing. The result obtained with this solver is

$$C_L = 0.077384$$

The last and the most appropriate method is the Vortex Lattice Method. This method assumes a 3D inviscid, incompressible flow over the wing. The wing is modeled by a sheet of lifting panels as given in Figure 4.18.

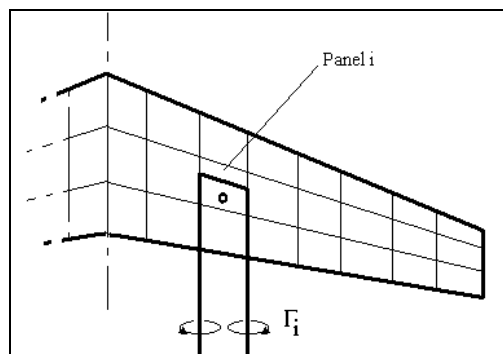


Figure 4.18. Lifting Panels

The theoretical details of the method are beyond the scope of this text, but detailed information about the Vortex Lattice Method can be found in [20] and [22]. The snapshot of the program used is given in Figure 4.19.

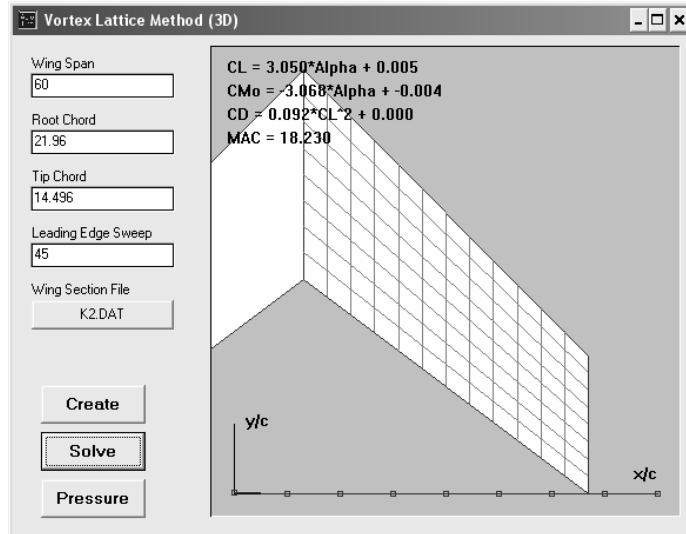


Figure 4.19. Vortex Lattice Method Solver [22]

As it can be seen from the figure, the total lift coefficient for the wing is given as a function of AOA.

$$C_L = 3.050 \times \alpha + 0.005$$

Using this expression with an AOA value of $\pi/180$ rad (1°), the total lift coefficient C_L is

$$C_L = 0.0582$$

These results are all crude approximations for the steady flow total lift coefficient. As stated above, the peak unsteady coefficient is expected to be higher than the steady coefficient. The variation of unsteady C_L with 2° of tip AOA, calculated from USER3D is given in Figure 4.17. The peak value is

$$C_L = 0.072$$

which is 24% higher than the vortex lattice value. The magnitude is in the correct side, but no other comment can be made about the results.

4.8 Force Calculation on the Structural Model

The next step is to calculate the loading on the structural model. The pressure distribution calculated will be transformed to the structural model using surface interpolation. The pressure distribution on the CFD mesh will be input as the source surface and pressure at the structural nodes will be interpolated. Since the AGARD Wing 445.6 is a slender wing, it is assumed that the normal direction of the surface is coincident with z-direction at all nodes. The surface interpolation routine selected for the mode shape transformation will be used in pressure transformation also. The pressure distribution calculated from the Euler variables given in Eq. (4.3) is non-dimensional and it will be dimensionalised according to Eq. (4.4). Afterwards, the force distribution on the structural nodes will be calculated using the interpolated pressure distribution.

The pressure distribution on the upper surface of the wing when the structure is at zero deflection is given in Figure 4.20. The pressure distribution plot on the wing surface does not change significantly in time. Since the oscillations are very small compared to the thickness of the wing, the pressure oscillates in a range of hundreds of Pa. However, as it can be observed from Figure 4.20 the pressure on

the wing surface is around 27,000 Pa. The sinusoidal lift variation in time is observed from both the total lift coefficient history and local pressure history variations on the wing.

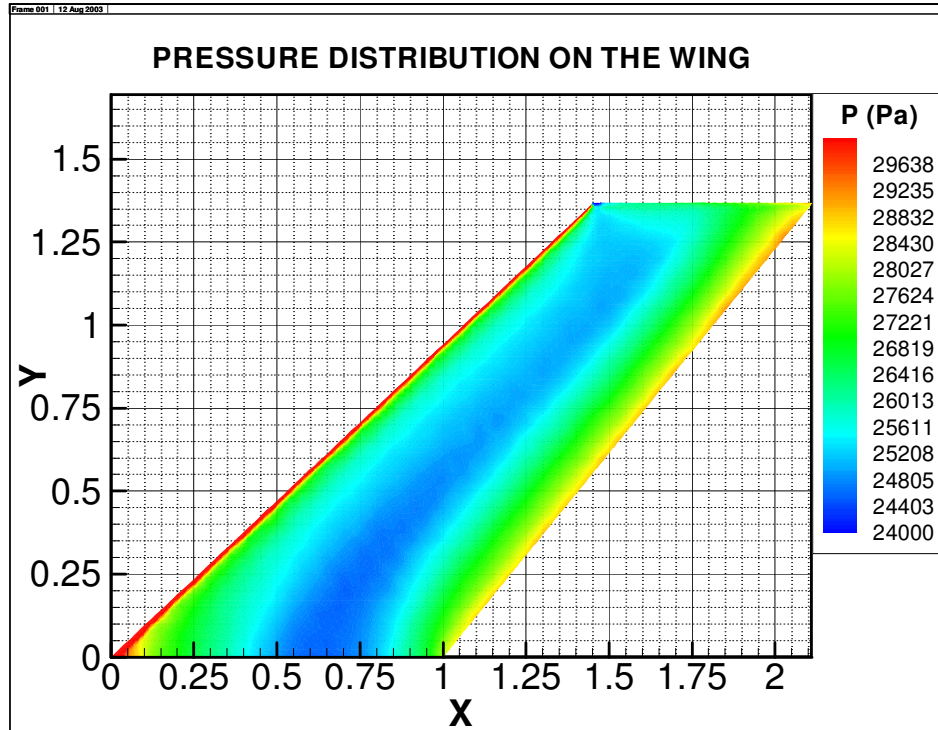


Figure 4.20. Pressure Distribution on the Upper Surface at Zero Deflection

As stated before, the pressure transformation is done with the same interpolation routine [15] used for mode shape transformation. In order to calculate the pressures at the 231 structural nodes, the pressure at the midpoint point of each structural mesh element was interpolated. Using the midpoint pressure values, forces at the nodes were calculated as shown in Figure 4.21 where A, B, C and D are the partial element surface areas adjacent to the node. In order to verify the pressure transformation, the pressure distribution on the wing was compared between the CFD mesh and the structural model.

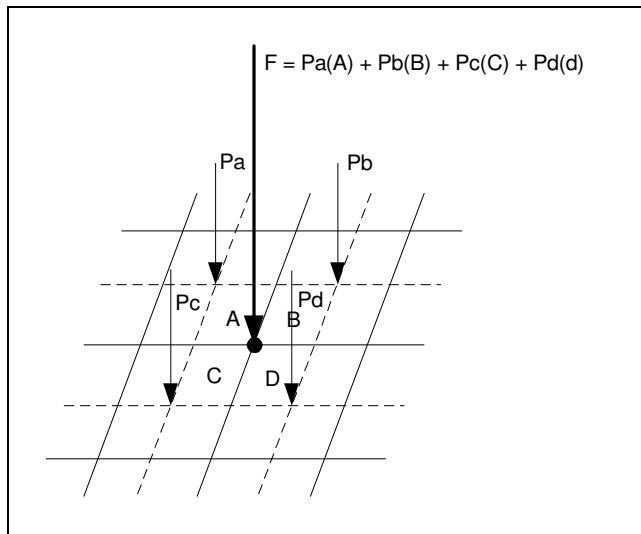


Figure 4.21. Nodal Force Calculation

In Figure 4.22 the pressure distribution on the upper side of the wing from CFD analysis is given for the wing at zero deflection. As it can be observed from the figure, pressure surface is quite a smooth surface for interpolation. The maximum surface derivatives occur in a narrow region at the leading edge of the structure. Since there are no structural nodes at the leading and trailing edges of the wing, there will be no interpolation points at these locations. Since a detailed error analysis of the interpolation routine DSURF was carried out in the mode shape interpolation process, the same study will not be repeated here again. However, the pressure contours calculated on the CFD mesh and interpolated on the structural mesh will be compared.

In Figure 4.23 the pressure distribution on the wing at four mode shapes with their corresponding natural frequencies at maximum deflections are given. The red lines are the pressure contours from CFD mesh whereas the blue lines are the pressure contours from the structure mesh. These contours are drawn at the peak structural deflections for all modes at the upper surface of the wing. In contrast to the mode shape transformation, there exist noticeable differences between contour lines.

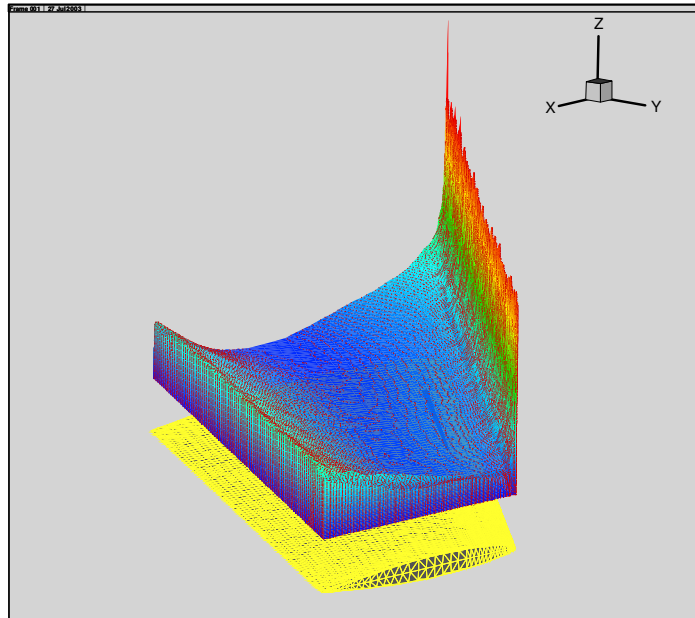


Figure 4.22. Pressure Surface at Zero Deflection

There are 231 nodes for the structural model and 6667 nodes for the CFD model. 207 of 6667 nodes are located at the leading and trailing edges of the wing. Remaining 6460 nodes are separated equally between upper and lower sides. Considering that 3437 nodes constitute the original pressure surface for each side of the wing, when transformed to 231 nodes, the same precise distribution can not be obtained any more. However, the transformation of mode shapes, from 231 nodes to 3437 nodes naturally conserves the accuracy of the surface all over the wing. As a result of the above discussion, it is judged that the interpolation routine developed by Akima [15] can also be used for pressure transformation between CFD mesh and structural model.

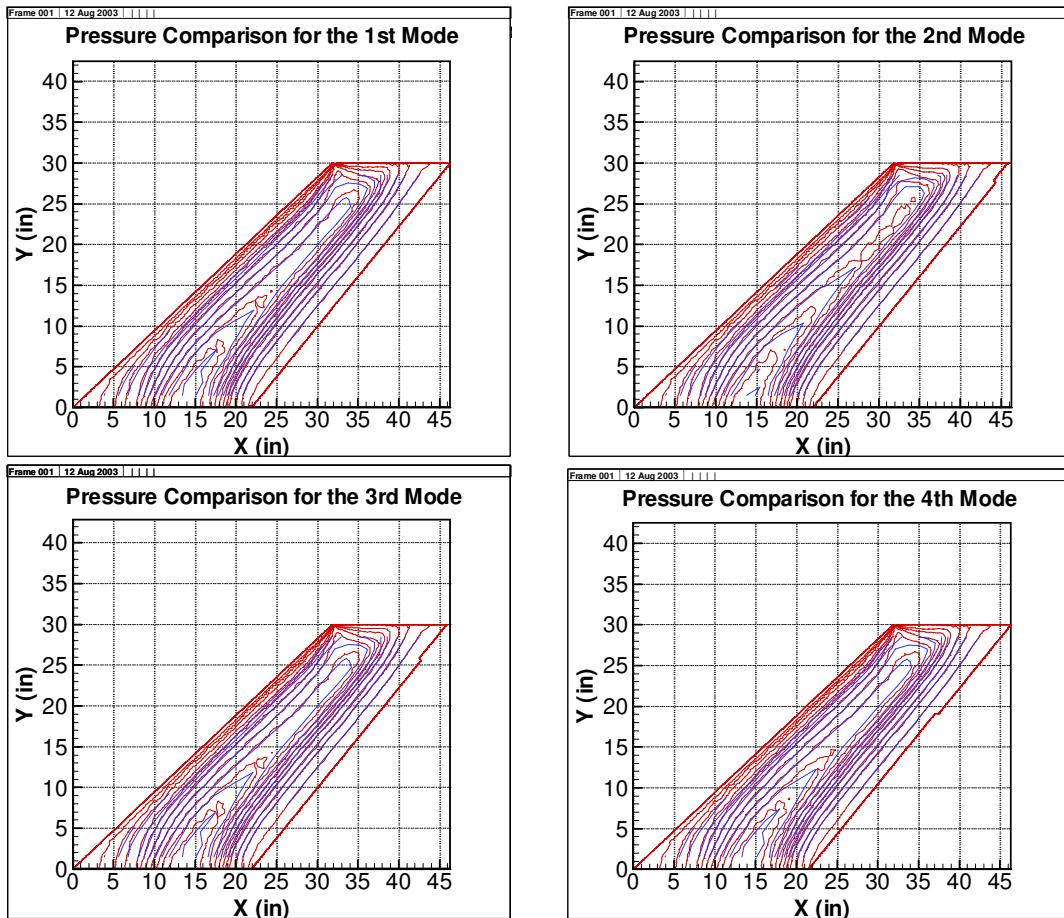


Figure 4.23. Pressure Comparison Between CFD Results and Interpolated Values

The force distribution on the structural model is calculated as explained in Figure 4.21. The pressure distributions on the upper and lower sides of the wing are interpolated separately at the structural nodes and the force distribution for upper and lower sides is calculated. As stated before, the surface normal direction all over the wing is assumed to be coincident with the z-direction. Therefore, the forces calculated at the upper and lower sides are directly summed vectorially to compute the resultant forces on the wing.

In Figure 4.24, the pressure differences between the upper and lower wing surface are given for all modes at their corresponding natural frequencies. From Figure 4.24, it is clear that the 2nd mode has the maximum total lift coefficient.

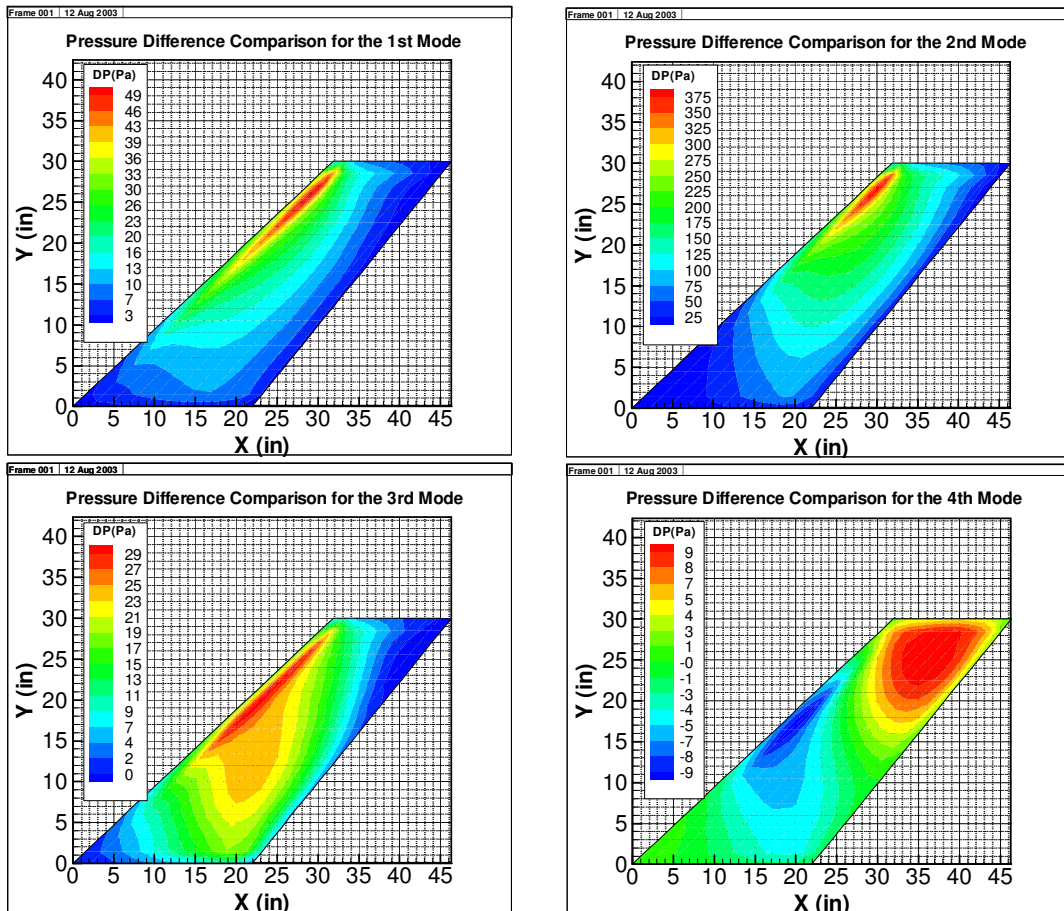


Figure 4.24. Pressure Difference Comparison

Also, comparing the 1st and 3rd modes, it can be seen that although the pressure difference for the 3rd mode is lower than that of the 1st mode, the pressure difference for the 3rd mode is much more distributed compared to the 1st mode. This fact also supports the condition given in Figure 4.12, that the 1st and 3rd mode C_L values are almost coincident. Also as discussed above, the total lift coefficient C_L for the 4th mode is very small. This can be explained again from Figure 4.24. The maximum pressure difference for the 4th mode is the lowest among all (9 Pa), in addition, the pressure difference distribution on the wing is such that the minimum pressure difference is -9 Pa, which causes the total C_L to be around

zero. The force distribution is calculated using the pressure distribution given above.

After transformation of the pressure surface from the CFD mesh to the structural mesh, there was a decrease in the accuracy of the distribution. While calculating forces, the pressures at the midpoints of elements are multiplied with large areas compared to CFD mesh element areas. It is thought that this procedure also causes some loss of accuracy in the method. In Figure 4.25, the total lift coefficient (C_L) is compared between the results obtained from USER3D and force calculation on the structural mesh.

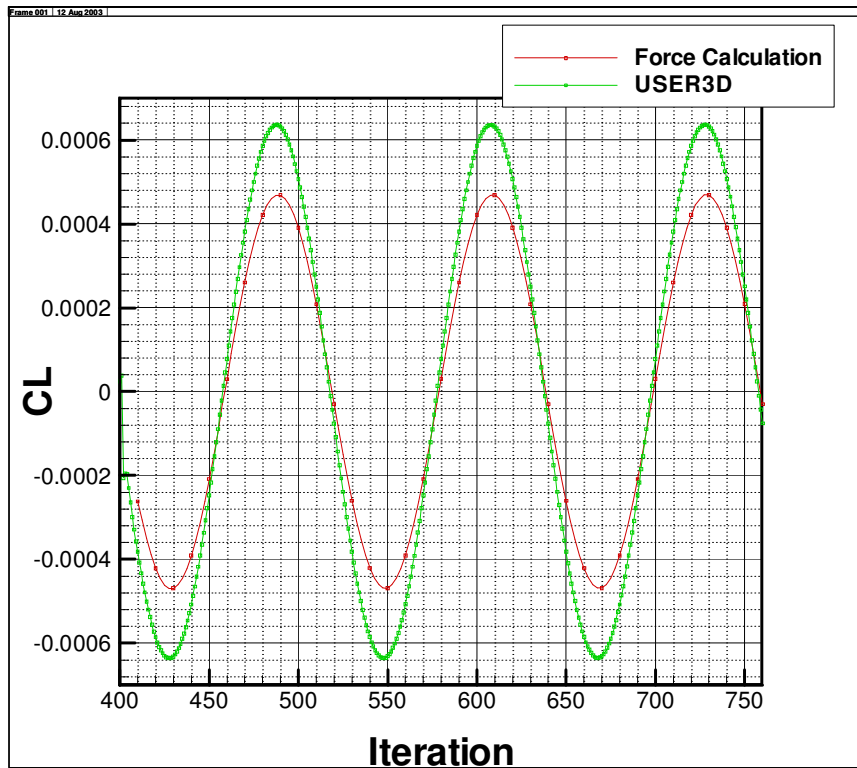


Figure 4.25. Comparison of Total C_L

It is seen that there is an error of approximately 25% between the two solutions. Since the main reason for this case was thought to be crude integration over the

structural mesh, the number of integration points in chordwise direction was increased from 10 to 80. That is, instead of considering the pressure at the center of each element (P_a , P_b , etc. in Figure 4.21), pressure values at 8 points on each element were considered. However, the total C_L curve and the force distribution did not change significantly. Therefore, it is thought that, the pressure surface obtained from the CFD model is the main reason for the error. As explained above, the pressure distribution on the CFD model was assumed to be acting in z-direction.

4.9 Aerodynamic Loading on Structural Model

In the previous section, the aerodynamic force distribution on the structural model was calculated. In this section, the variation of force with frequency and mode shape will be investigated. There is phase difference between structural oscillations and aerodynamic forces. As it can be observed from Figure 4.26, the phase difference is different for each node. As explained in chapter 3, there are 21 nodes in spanwise direction and 11 nodes in chordwise direction. The numbering starts from the node at root of leading edge and increases in spanwise direction. After 21st node at the tip of leading edge, 22nd node is at the second spanwise line of nodes and it is at the root of the wing. In Figure 4.26, the phase angle variation for all four modes and ten frequencies are given. For detailed investigation of results the phase angle variation of first mode is given in Figure 4.27. It is clearly observed that the phase angle variation in spanwise direction is much more significant compared to the phase angle variation in chordwise direction. This shows the relation between the sectional AOA and phase angle since the sectional AOA variation given in Figure 4.13 shows that sectional AOA changes rapidly from root to tip for the first mode. Also it is seen from Figure 4.27 that there is a direct relation between the oscillation frequency and phase.

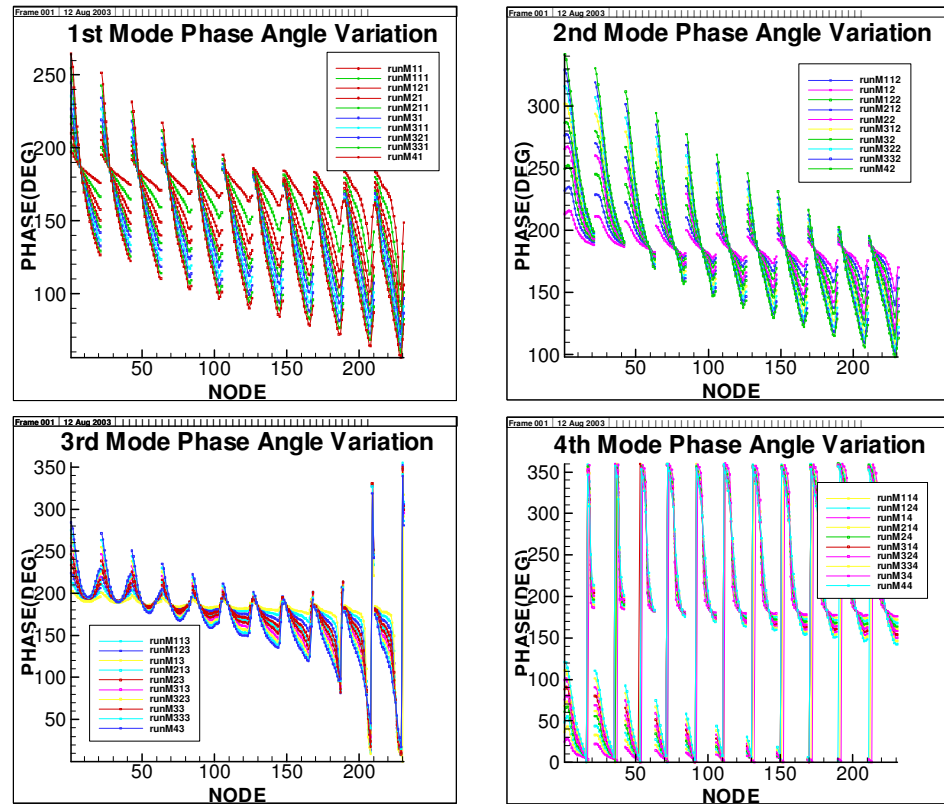


Figure 4.26. Phase Angle Variation on the wing

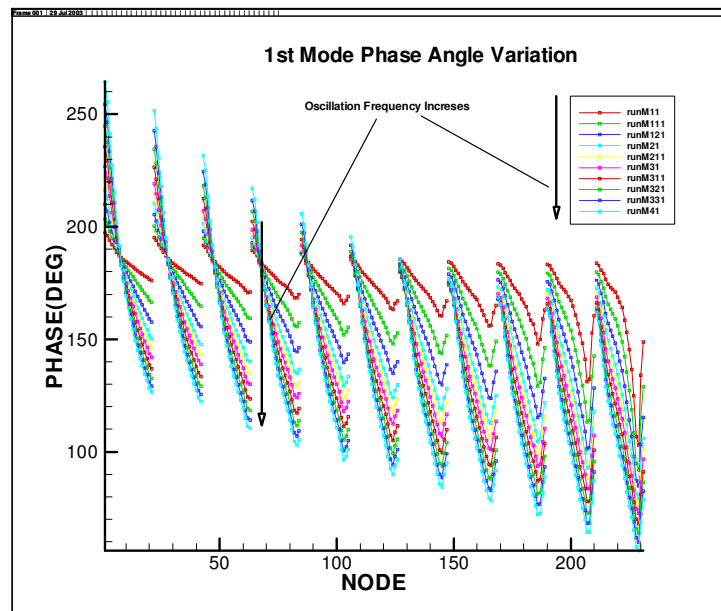


Figure 4.27. 1st Mode Phase Angle Variation

The change in direction of relation between the oscillation frequency and the phase angle is thought to be because of local AOA changes at that node. The oscillations are quite small such that deflections due to oscillation are smaller than the airfoil thickness. Similar behavior can also be observed for the other mode shapes also. To check that such small deflections are not within the numerical noise, unsteady aerodynamic loads were computed with the modal deflections increased by 100-fold. The computed results also increased very nearly 100-fold.

CHAPTER 5

NUMERICAL SOLUTION

5.1 Introduction

In this chapter, the application of the procedure described in Chapter 2 will be explained. The first step of the procedure was to carry out the modal analysis of the AGARD Wing 445.6 as explained in Chapter 3. The results obtained from modal analysis are compared with an experimental study [9] and the results of previous studies [10]. Next, the CFD solution was done for the first four mode shapes with harmonic oscillations as explained in Chapter 4. Using the CFD analysis results, pressure distributions on the wing surface were calculated. Using surface interpolation [15], the pressure distributions are transferred to the structural model. Using the transformed pressure distributions, force distributions on the structural model are calculated.

It was observed that there is phase difference between the oscillation of the wing and the aerodynamic forcing at each node. The aerodynamic force distribution was represented in complex terms and using the integration procedure given in Chapter 2, real and imaginary parts were obtained.

5.2 Solution Procedure

The theoretical formulation of the method proposed by Akgün [16] was explained in Chapter 2. In this section, the numerical solution procedure will be explained as shown in Figure 5.1.

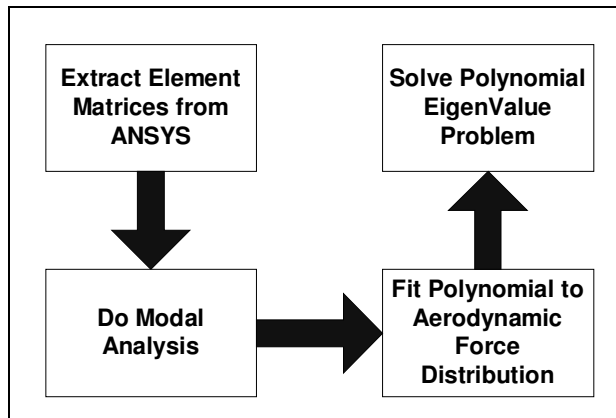


Figure 5.1. Numerical Solution Procedure

The first step of the procedure is to get the modal mass and stiffness matrices of the AGARD Wing 445.6. The User Programmable Features (UPF) of ANSYS was used to get these matrices.

After the finite element model of the wing was constructed, whole model was transformed to a superelement. The superelement in ANSYS is a group of previously assembled ANSYS elements that is treated as a single element which is a mathematical matrix representation of an arbitrary structure. It does not need to have a geometrical shape and it is obtained from a substructuring analysis in ANSYS [23]. The mass and stiffness matrices of the superelement become the mass and stiffness matrices of the system.

Since all degree-of-freedoms of nine nodes at the root were fixed, the superelement actually contains 222 nodes. In addition, the rotation around z-axis was also constrained at all nodes on the wing, so there are five degrees-of-freedom at each node. As a result, the size of the mass and stiffness matrices is $[1110 \times 1110]$. The remaining part of the numerical solution was completed using MATLAB[®]. The first step is to carry out a modal analysis as explained in Chapter 3 with MATLAB[®]. The mode shapes and natural frequencies obtained are compared with the solution obtained from ANSYS[®].

Table 5.1. Comparison of Natural Frequencies

Mode #	ANSYS	MATLAB
1	9.688	9.688
2	37.854	37.854
3	50.998	50.998
4	92.358	92.358

As given in Table 5.1, the natural frequencies calculated from both analyses strictly agree with each other as expected. In addition, the mode shapes given in Figure 5.2 are in very good agreement with the mode shapes given in Chapter 3 (Figures 3.3-3.11). These results show that the element matrices extracted from ANSYS[®] and the modal analysis function written in MATLAB[®] are correct.

The next step is polynomial curve fitting to aerodynamic force distribution on the wing according to Eqs. (2.34) and (2.35). The order of the polynomial fit must be at least 2nd order since the coefficient of the mass matrix is of order two. In order to determine the order of polynomial fit, 2nd, 3rd, 4th and 5th order polynomial fits are tried and it was observed that the resulting flutter frequency did not change

significantly. As a result, it was decided to use a 3rd order polynomial fit to aerodynamic forcing defined by ten points.

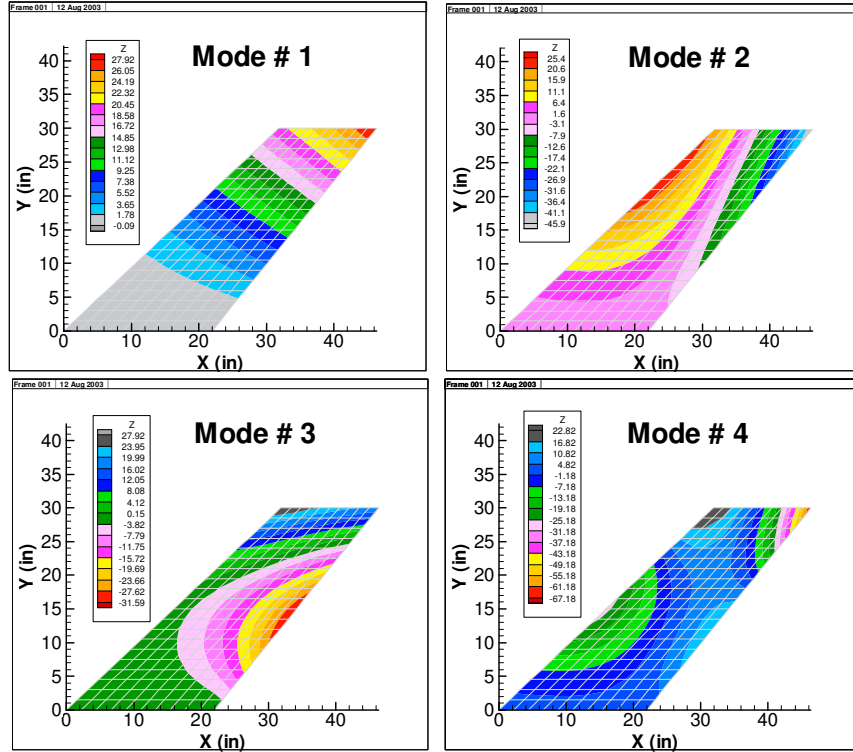


Figure 5.2. Mode Shapes Calculated from MATLAB

There are 231 nodes on the structural model, and the CFD solution is carried out at ten different frequencies for four mode shapes of the structure. Although the finite element model extracted from ANSYS® contains 222 nodes, pressure and force calculation are done at all 231 nodes. There are totally 40 aerodynamic force data at each node. These are stored as real and imaginary parts of aerodynamic loading as defined by Eq. (2.33). The real and imaginary parts of raw aerodynamic data calculated at 231 structural nodes are stored in separate 3 dimensional matrices

$$[FR]_{i,j,k} \text{ for the real part} \quad (5.1)$$

$$[FI]_{i,j,k} \text{ for the imaginary part} \quad (5.2)$$

where, i : number of modes (4)

j : number of nodes (231)

k : number of frequencies(10)

For the real and imaginary parts, a 3rd order polynomial ($c_0k^3 + c_1k^2 + c_2k + c_3$) in terms of reduced frequency was fit to the 10 data points at every 231 node and all 4 modes. As a result, 4 polynomial coefficients for every 40 case were calculated and stored in accordance with Eqs. (2.34) and (2.35).

$$\begin{bmatrix} T^l \end{bmatrix} = \begin{bmatrix} t_{1,1}^l & \cdots & t_{1,n}^l \\ \vdots & \ddots & \vdots \\ t_{231,1}^l & \cdots & t_{231,n}^l \end{bmatrix} \quad \text{for the real part} \quad (5.3)$$

$$\begin{bmatrix} Z^l \end{bmatrix} = \begin{bmatrix} z_{1,1}^l & \cdots & z_{1,n}^l \\ \vdots & \ddots & \vdots \\ z_{231,1}^l & \cdots & z_{231,n}^l \end{bmatrix} \quad \text{for the imaginary part} \quad (5.4)$$

where, l : order of coefficient (0...3)

n : number of mode shapes (4)

In order to verify the accuracy of the polynomial fit, the discrete data computed is plotted together with fitted polynomial for the 11th node of 2nd mode shape in Figure 5.3. It can be seen from the figure that polynomial fit is in good agreement with the computed data.

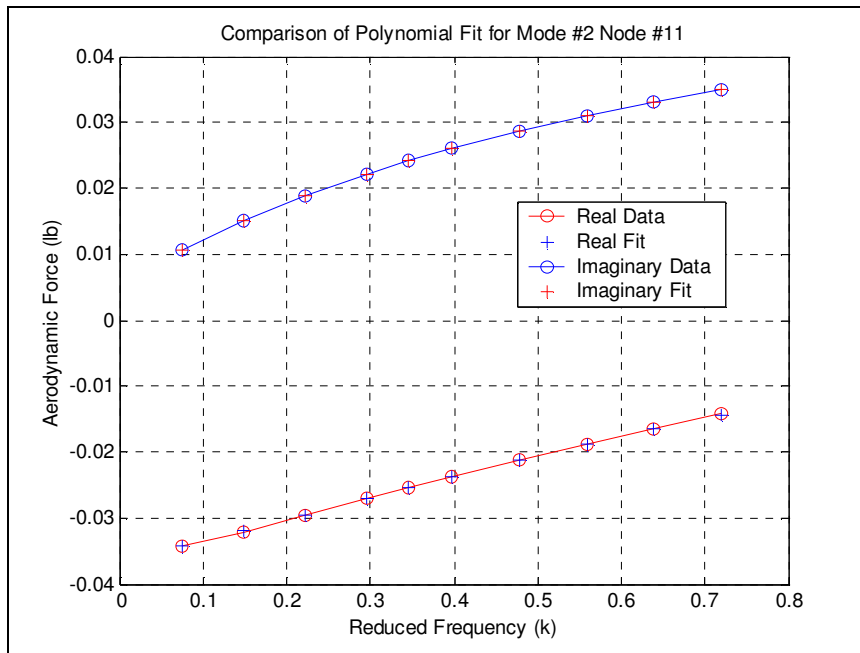


Figure 5.3. Polynomial Fit Comparison

The real and imaginary polynomial coefficient matrices are reduced to (222×4) in order to achieve accordance with element matrices extracted from ANSYS[®]. The resultant polynomial system is defined by Eqs. (2.38), (2.39) and (2.40). After premultiplying the polynomial coefficient matrices by the transpose of mode shape matrices $([\Phi]^T)$ we obtained (4×4) matrices for real and imaginary parts. However, the Q matrices defining the polynomial coefficients in Eq. (2.38) are (8×8) since the original (4×4) complex problem was expanded for real analysis.

Since the unsteady aerodynamic forces are the resultant forces due to the harmonic motion of the wing, the “ c_3 ” term for the imaginary part which corresponds to zero oscillation frequency was expected to be zero. However, it was seen that these terms are not necessarily close to zero. Therefore, the 0th order term was included in the polynomial eigenvalue problem.

The real and imaginary generalized aerodynamic forces (GAF) are obtained from

$$[A_R] = [\Phi]^T [T] \quad (5.5)$$

$$[A_I] = [\Phi]^T [Z] \quad (5.6)$$

where, $[T]$ and $[Z]$ are calculated at a reduced frequency from

$$[T] = [T^3]k^3 + [T^2]k^2 + [T^1]k + [T^0] \quad (5.7)$$

$$[Z] = [Z^3]k^3 + [Z^2]k^2 + [Z^1]k + [Z^0] \quad (5.8)$$

The distribution of generalized aerodynamic forces with respect to reduced frequency is given in Figure 5.4. It can be observed from the figure that imaginary parts always tend to zero, whereas the real part of the GAF does not. This behavior of GAFs also coincides with the figures given in References 8,19. Since the Mach number for which these graphs are plotted is different, the GAF distributions are also different with respect to reduced frequency. Besides, the amplitudes of oscillations for each mode used in present study, which is 0.0015 – 0.03 inches, is very small compared to those used in the References which is ~0.5 inches. As a result, the order of magnitude of GAFs between the references and the present study is quite different. However, the element matrices are transformed to modal matrices using the mode shape matrices with small amplitudes calculated in present study and the aerodynamic loads are also premultiplied by the same mode shape matrices. As a result, the affect of amplitude of oscillation is eliminated.

Using the above explained procedure, the flutter frequency of AGARD Wing 445.6 at 0.678 Mach is calculated as using 2nd, 3rd, 4th, and 5th order polynomial fits. As shown in Table 5.2, the resultant flutter frequency did not change significantly.

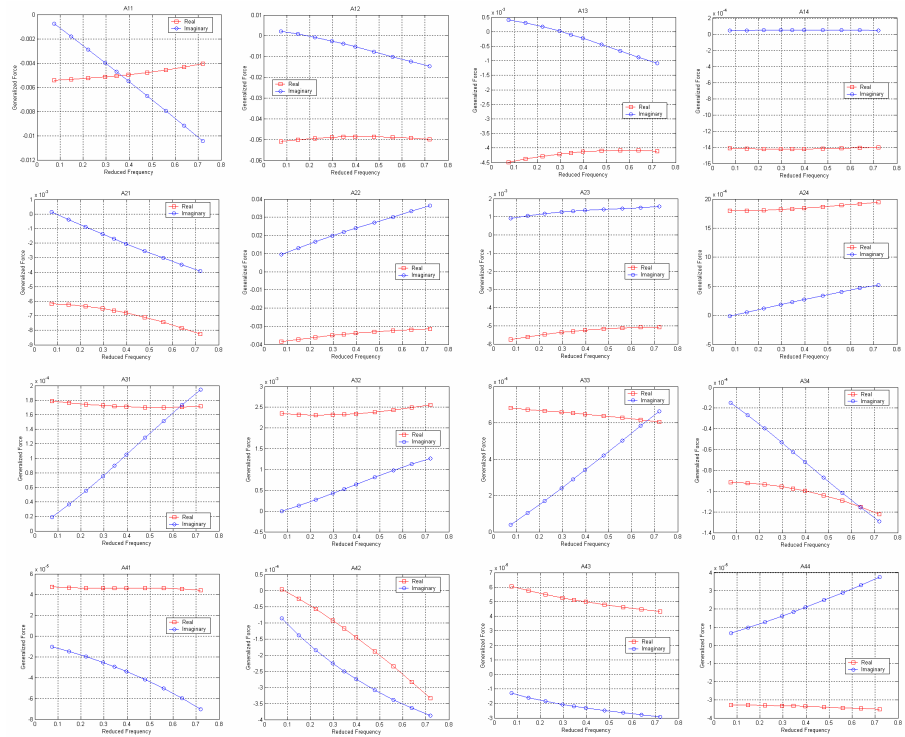


Figure 5.4. Generalized Aerodynamic Forces for the first four structural modes at
 $M_\infty = 0.678$

Table 5.2. Comparison of Polynomial Fit Order

Order of Polynomial Fit	Flutter Frequency (rad/s)
2	82.6957
3	82.6897
4	82.6741
5	82.6577

The resultant flutter frequency calculated using 3rd order polynomial fitting is compared with the experimental result [9] in Table 5.3.

Table 5.3. Flutter Frequency Comparison

Mach	Present Study	Experimental Result [9]	Error
0.678	82.6897 (rad/s)	113.0 (rad/s)	% 26.8

The same solution has been carried out once again by using the amplitude of oscillations the same as given in References 8,19. However, the calculated flutter frequency, which is given below, did not change significantly as expected.

$$\omega_F = 82.58 \text{ (rad/s)}$$

CHAPTER 6

CONCLUSIONS AND RECOMMENDATIONS

In this thesis, a new approach to the solution of flutter problem was applied to AGARD Wing 445.6, the first AGARD standard aeroelastic configuration for dynamic response [9]. The results of the modal analysis of AGARD Wing 445.6 were compared with the experimental values [9] and the results of the previous studies [10]. It was shown that the results of the modal analysis were in good agreement with the experimental results.

The CFD analysis showed, as expected, that there is phase difference between the oscillation of the wing and aerodynamic forces and also between oscillations of all nodes of the wing.

The approach used in this study is very similar to classical V-g method solutions [8], [19]. However, an iterative solution procedure is required for the identification of flutter frequency with these methods. In the present case, the flutter frequency is obtained through the solution of an eigenvalue problem.

With the approach here, the time consumed for the determination of flutter frequency for a structure is decreased significantly. Observing the generalized aerodynamic force functions given in References [8], [19] and in present study, it is judged that polynomial curve fitting is suitable for representing the aerodynamic forces in terms of the reduced frequency. However, the method introduced a significant error compared to the experimental results [9]. The main cause of this

error is thought to be due to the accuracy of the force calculation. The total lift coefficient comparison has shown that, although the pressure surface is quite a smooth one, the force calculation on the wing introduced a significant error.

However, the solution for the AGARD Wing 445.6 was obtained at only 0.678 Mach. In order to obtain a complete and comparable validation, the solution should be repeated at the experimental flow conditions given in Reference [9] and the force calculation procedure should be considered again. Besides, it is thought that repeating the CFD solutions with the amplitudes specified at References [8] and [19] would help in comparing the accuracy of the aerodynamic solution since there is no experimental data about the generalized aerodynamic force.

Each CFD run for this method takes around 40~45 wall clock minutes which is quite low compared to coupled solutions [19]. Since the total time needed for force calculation and eigenvalue problem solution is around couple of minutes, the approach considered saves considerable time compared to the coupled methods. This is an advantage in aeroelastic optimization studies in particular where a flutter analysis needs to be performed in every cycle of optimization.

REFERENCES

1. Bisplinghoff R. L., Ashley H., Halfman R. L., *Aeroelasticity*, 1957, Addison-Wesley Publishing Company.
2. Theodorsen T., “General Theory of Aerodynamic Instability and the Mechanism of Flutter”, *NACA Report 496*, 1935.
3. Theodorsen T., Garrick, I. E., “Mechanism of Flutter A Theoretical and Experimental Investigation of the Flutter Problem”, *NACA Report 685*, 1940.
4. Ashley H., Zartarian G., “Piston Theory – A New Aerodynamic Tool for the Aeroelastician”, Twenty-Fourth Annual Meeting, IAS, New York, January 23-26, 1956.
5. Yates E. C., “Modified-Strip-Analysis Method for Predicting Wing Flutter at Subsonic to Hypersonic Speeds”, *Journal of Aircraft Vol. 3, No. 1*, 1966.
6. Slone A. K., “A Finite Volume Unstructured Mesh Approach to Dynamic Fluid Structure Interaction between Fluids and Linear Elastic Solids”, *Ph.D. Thesis*, 2000, University of Greenwich, London, UK.
7. Lee-Rausch, E. M., Batina, J. T., “Wing Flutter Boundary Prediction Using Unsteady Euler Aerodynamic Method”, *Journal of Aircraft, Vol. 32, No. 2*, 1995.
8. Lee-Rausch, E. M., Batina, J. T., “Calculation of AGARD Wing 445.6 Flutter Using Navier-Stokes Aerodynamics”, *AIAA-93-3476*, 1993.

9. Yates E. C., “AGARD Standard Aeroelastic Configurations for Dynamic Response I – Wing 445.6”, *AGARD Report No. 765*, 1985.
10. Kolonay, R. M., “Computational Aeroelasticity”, RTA-NATO *The Applied Vehicle Technology Panel*, 2001.
11. Zhenyin Li, “Parallel Computations of 3D Unsteady Compressible Euler Equations with Structural Coupling,” http://www.engr.iupui.edu/me/courses/li_thesis2_summer02.ppt
12. Oktay, E., “USER3D, 3-Dimensional Unstructured Euler Solver,” ROKETSAN Missile Industries, Inc., SA-RS-RP-R 009/442, Ankara, Turkey, May 1994.
13. Oktay E., Akay H. U., Uzun A., “A Parallelized 3D Unstructured Euler Solver For Unsteady Aerodynamics”, *AIAA-2001-0107*, 2002.
14. Akay, H. U., Oktay E., Li Z., He X., “Parallel Computing For Aeroelasticity Problems,” AIAA Paper 2003-3511, 33rd AIAA Fluid Dynamics Conference, June 23-27, 2003, Orlando, Florida, United States.
15. AKIMA, H. A method of bivariate interpolation and smooth surface fitting for irregularly distributed data points. *ACM Trans. Math. Software* 4, 2 (June 1978), 148-159.
16. Akgün M. A., “An Approach To Uncoupled Flutter Calculation” *Paper Submitted to AIAA Journal*.
17. <http://www-unix.mcs.anl.gov/mpi/mpich/indexold.html>
18. <http://www.ae.metu.edu.tr/resource/linux>
19. Liu F., Cai J., Zhu Y., Wong A.S.F., Tsai H. M., ‘Calculation of Wing Flutter by a Coupled CFD-CSD Method’, *AIAA-2000-0907*, 2000.
20. Anderson J. D., *Fundamentals of Aerodynamics 2nd Ed.*, 1991, McGraw-Hill International Editions.

21. Kaya, M. “spot.f, A Panel Code for Inviscid, Incompressible and Irrotational Flow Over Airfoils”, AE 443 Project I, Department of Aerospace Engineering, Middle East Technical University, 1999
22. <http://www.aero.usyd.edu.au/aero/vlm/vlm.html>
23. ANSYS Online Help Documentation

APPENDIX A

LIFT COEFFICIENT VARIATIONS

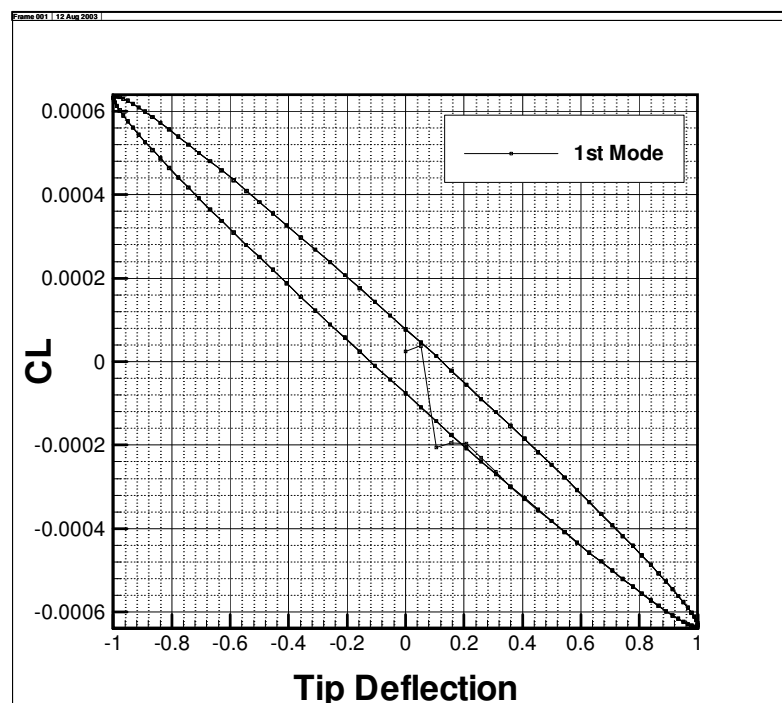


Figure A.1. The 1st Mode Lift Coefficient Variation with Tip Deflection

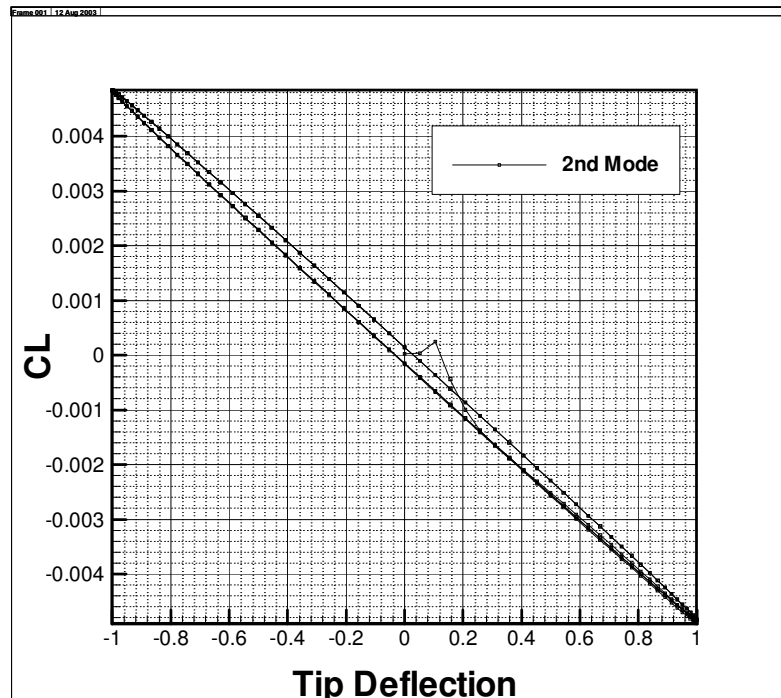


Figure A.2. The 2nd Mode Lift Coefficient Variation with Tip Deflection

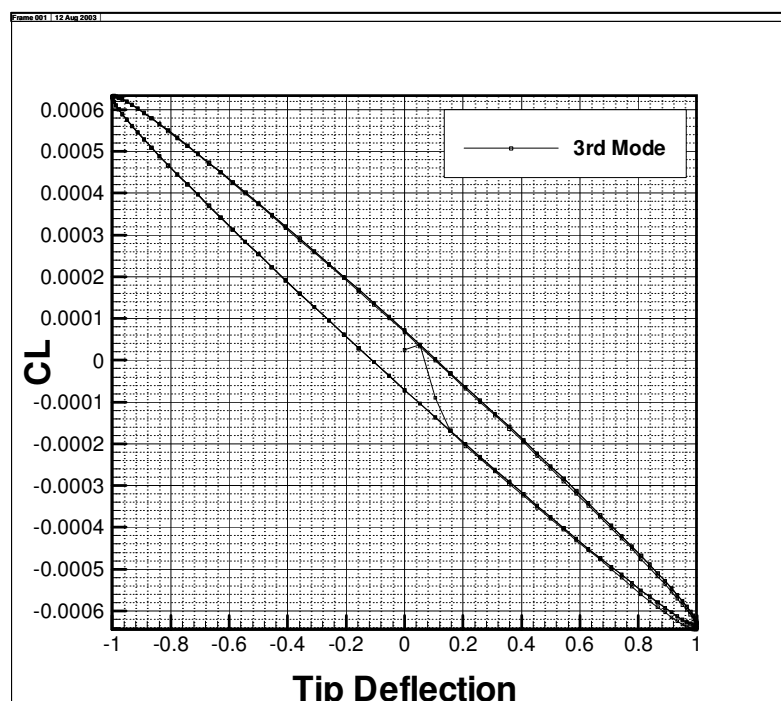


Figure A.3. The 3rd Mode Lift Coefficient Variation with Tip Deflection

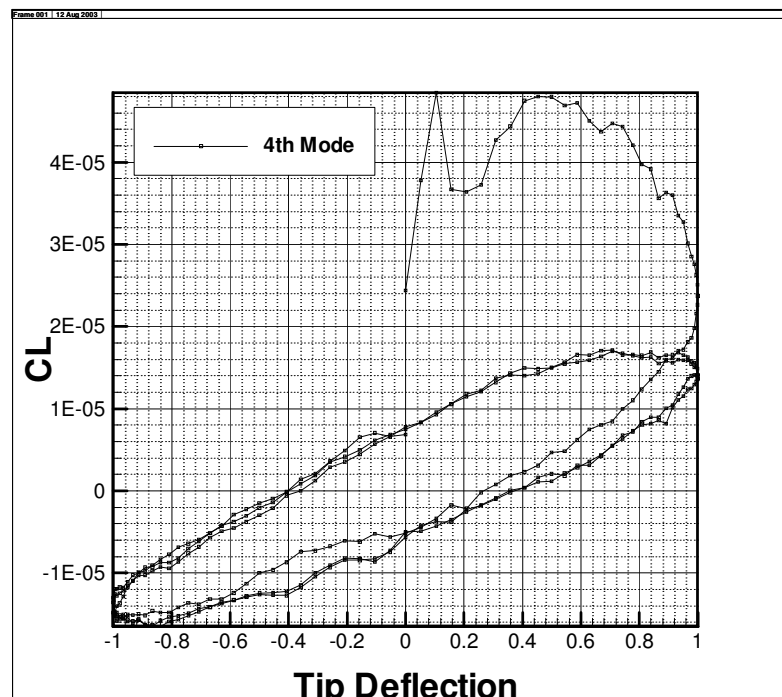


Figure A.4. The 4th Mode Lift Coefficient Variation with Tip Deflection

APPENDIX B

ANSYS FINITE ELEMENT MODEL MACRO FILE

```
/BATCH
/COM,ANSYS RELEASE 7.0 UP20021010    12:40:30  04/13/2003
/input,menustmp,",,,,,,,,,,1
/GRA,POWER
/GST,ON
/PLO,INFO,3
/GRO,CURL,ON
/REPLOT,RESIZE
/REPLOT,RESIZE
/FILNAME,AgardModal,0
/REP7
!*
/units, bin
!*
ET,1,SHELL63
!*
/input, ansys_real,inp,,
!*
MPREAD,'mat','mat',''
!*
NRRANG,1,99999999,1,
NREAD,'NodesKolonay_BIN','txt',''
!*
ERRANG,1,99999999,1,
EREAD,'ElementKolonay','elm',''
!*
!*
ANTYPE,2
MSAVE,0
!*
MODOPT,LANB,4
```

```
EQSLV,SPAR
MXPAND,4, , ,0
LUMPM,0
PSTRES,0
!*
MODOPT,LANB,4,0,0, ,ON
FLST,2,231,1,ORDE,2
FITEM,2,1
FITEM,2,-231
!*
/GO
D,P51X, ,0, , , ,ROTZ, , , ,
FLST,2,9,1,ORDE,9
FITEM,2,22
FITEM,2,43
FITEM,2,64
FITEM,2,85
FITEM,2,106
FITEM,2,127
FITEM,2,148
FITEM,2,169
FITEM,2,190
!*
/GO
D,P51X, ,0, , , ,ALL, , , ,
FINISH
/SOL
/STATUS,SOLU
SOLVE
FINISH
!
LGWRITE,AgardModal,lgw,C:\USER\KORAYK\TEZ\ANALYSIS\ANSYS\AG
ARD_445.6\PLATE\KORAY\,COMMENT
SAVE
FINISH
```